THE SPATIAL CHIRP EFFECT AND DISPERSION LAW OF VIRTUALLY IMAGED PHASED ARRAY (VIPA) WAVELENGTH DEMULTIPLEXER

A Thesis
Submitted to the Faculty
of
Purdue University
by
Shijun Xiao

In Partial Fulfillment of the
Requirements for the Degree
of
Master of Science in Electrical and Computer Engineering

August 2003

This thesis is dedicated to my lovely wife Ms. Qinbo Qu for her great love and support.

AKNOWLEDGEMENTS

Thanks to my advisor Professor Andrew M. Weiner for his great guidance during all the research work. With his insightful perspective, I am able to work in such a fantastic area with many great discoveries. Thanks to my committee members Professor Daniel S. Elliott and Professor Michael R. Melloch for their support on this master thesis work. Thanks to Professor Vladimir M. Shalaev for the discussions on topics related to this thesis. Thanks to our group research engineer Daniel E. Leaird for his help on experiments. Thanks to our group member Jason D. Mckinney and Albert Vega for their help on the thesis's edition. We also appreciate Christopher Lin from Avanex Corporation for his donation of VIPA samples.

TABLE OF CONTENTS

Page

LIST OF FIGURES

ABSTRACT

Xiao, Shijun M.S.E.C.E., Purdue University, August 2003. The Spatial Chirp Effect and Dispersion Law of Virtually Imaged Phased Array (VIPA) Wavelength Demultiplexer. Major Professor: Andrew M. Weiner.

A modified Fabry-Perot etalon termed a virtually-imaged phased-array (VIPA) was recently introduced as a spectral disperser. With respect to common diffraction gratings with ~30 degree blaze angles, VIPA has a larger angular dispersion, lower polarization sensitivity, simpler structure, lower cost and compactness. Its applications for wavelength demultiplexing and chromatic dispersion compensation have been demonstrated.

An input beam is introduced into a VIPA etalon by focusing through an uncoated (or anti-reflection coated) region on the front-side reflector. The beam bounces back and forth between the two coatings resulting in multiple reflections. The name comes from the device operating as if there were multiple virtual sources interfering with each other as in a phased array. As in any phased array, the direction of the output beam depends on the phase difference between the array elements (virtual sources). Since this phase difference is frequency dependent, the direction of the output beam also varies with frequency; i.e., the VIPA functions as a spectral disperser.

We observe a novel spatial chirp effect, in which different spatial portions of the output beam from a Virtually Imaged Phased Array (VIPA) etalon contribute to different optical frequencies in its frequency demultiplexing response. We develop a theory that can fully explain the spatial chirp effect. We also demonstrate that the spatial chirp can be

controlled, and we can obtain a spatial chirp-free VIPA demultiplexer. In the case of spatial chirp-free VIPA, we propose a modified dispersion law, which is verified by us over the full operation region of VIPA.

1. INTRODUCTION

A new optical wavelength demultiplexer - the virtually-imaged phased-array (VIPA) was introduced recently and demonstrates several advantages over common diffraction gratings with ~30 degree blaze angle: large angular dispersion, low polarization sensitivity, simple structure, low cost and compactness. The application of the VIPA in wavelength division multiplexing (WDM) communication has been tested and demonstrated [1]. The VIPA with graded reflectivity was invented for low insertion loss and crosstalk in WDM [2]. Chromatic dispersion compensation (Fig. 1.4, Fig. 1.5) using the VIPA has also been demonstrated [3, 4]. According to US patent data, several patents have been issued for the VIPA [5, 6]. C. Lin studied chromatic dispersion compensation using the VIPA in his master thesis, where he mainly focused on the computation and design of the compensation system [7]. Our group member, A. Vega, has studied the dispersion law of the VIPA [8, 9], which is the first formal dispersion law proposed for the VIPA spectral disperser to our knowledge.

The VIPA is a modified Fabry-Perot etalon (Fig. 1.1). It consists of two glass plates. The transmission side is coated with a high-reflectivity film (>=95%); the other side is coated with an almost 100% reflectivity film except in the window area, which is uncoated or antireflection (AR) coated. If the etalon cavity is filled with air, it is called an air spaced VIPA; otherwise if it is filled with some glass of refractive index n, it is called a solid VIPA. A collimated laser source is focused with a cylindrical lens into the VIPA etalon. Due to the high reflection of the VIPA etalon, the laser beam experiences multiple reflections back and forth, and the multiple reflections result in multiple diverging output beams from the transmission plate. These output beams interfere with each other to form

collimated beams with different output angles depending on the wavelength with constructive interference. A thin lens is placed behind the VIPA to collect these collimated beams with different output angles, and fiber receivers are positioned in the confocal region after the lens to receive the laser power. This is a simple scheme for a wavelength demultiplexing system (Fig. 1.2). For more information on the VIPA structure and experiment setups, please refer to A. Vega's publications [8, 9].

Chapter 2 is about the detailed derivation for the important theoretical foundation of our demultiplexer theory and dispersion theory. We verify the equivalence between the Fresnel scalar diffraction integral and the paraxial wave equation for Gaussian beams [10, 11, 12, 13, 14]. The Fresnel scalar diffraction integral is another form of solution to the well known paraxial wave equation, and this means Gaussian beams can be described by the diffraction integral. A general lens transform has been derived from the diffraction integral, which is used to derive the VIPA demultiplexer theory and dispersion law with the assumption of Gaussian beams incident into VIPA. This part is also useful for describing the use of a VIPA in a direct space-to-time (DST) pulse shaper [15, 16, 17], which is a research topic for future work.

Chapter 3 can be traced back to the work on wavelength demultiplexing using the VIPA published by M. Shirasaki [1]. An interesting phenomena here is the asymmetric line-shape that can be noticed on the VIPA demultiplexer transmission spectra (Fig. 1.3). The asymmetry here means that a longer tail exists on one side of the transmission peak, which is obvious in the data from M. Shirasaki. The same phenomena was also observed by A. Vega [8, 9]. The topic of this part is to explain such asymmetric line-shape. We propose a theory that can fully explain the asymmetric effect demonstrated in experiments. We identify a new effect called spatial chirp as the cause of the line-shape asymmetry and broadening [18]. In addition to the discussion on spatial chirp and broadened asymmetric line-shapes, we also show from our demultiplexing theory how symmetric line-shapes without spatial chirp can be obtained, and we confirm this through experiments. These symmetric line-shapes have a smaller full width half maximum

(FWHM). For application in WDM systems, zero spatial chirp is preferred, which results in a line-shape with narrow FWHM and low inter-channel cross talk.

Chapter 4 compares the newly proposed dispersion law with that proposed by Vega and Weiner [8, 9]. For the VIPA with zero spatial chirp, we propose a new dispersion law compared to that of Vega and Weiner. In contrast to the dispersion law of [8, 9], which we show is valid only for sufficiently large incident angles, our new dispersion theory describes the VIPA behavior for all possible incident angles including small angles. The new dispersion law is valid under the paraxial approximation, and it demonstrates a nontrivial dispersion relation that depends on the second order of output angles, which isn't shown in the Vega-Weiner dispersion theory. This difference is always obvious when the dispersion on first order is balanced with the dispersion on the second order, where the order refers to the Taylor series order of output angle. Also in M. Shirasaki's publications, he only mentioned a few simple expressions for the angular dispersion [1]. Here we derive the angular dispersion relations by complete theoretical analysis, which we confirm by several experiments with different conditions. Complete theory and experiments about our new spectral dispersion law are presented in this thesis.

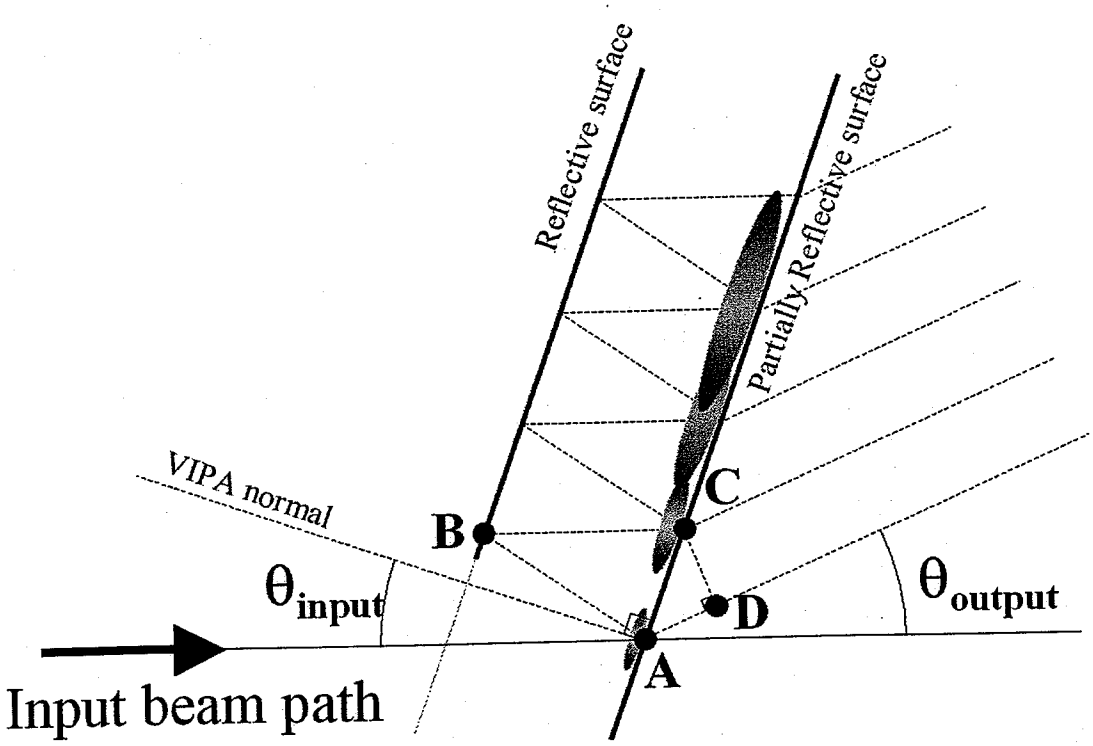

Fig. 1.1. Schematic diagram of an air-spaced VIPA [8, 9]

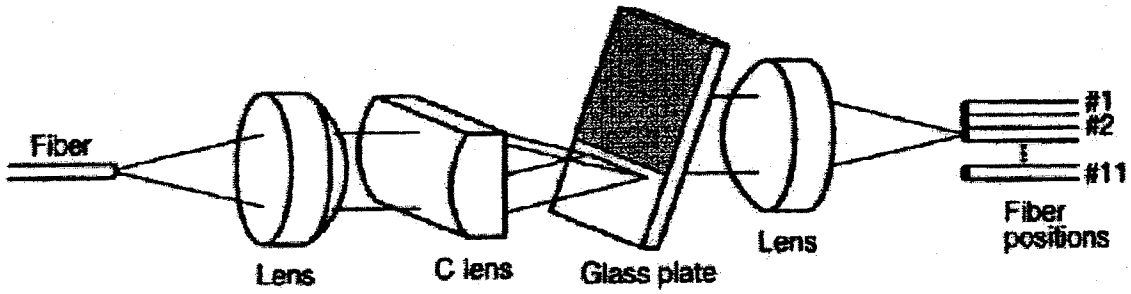

Fig. 1.2. Schematic of the VIPA wavelength demultiplexer from [1]

The collimated light from the glass plate is focused into the output fiber.

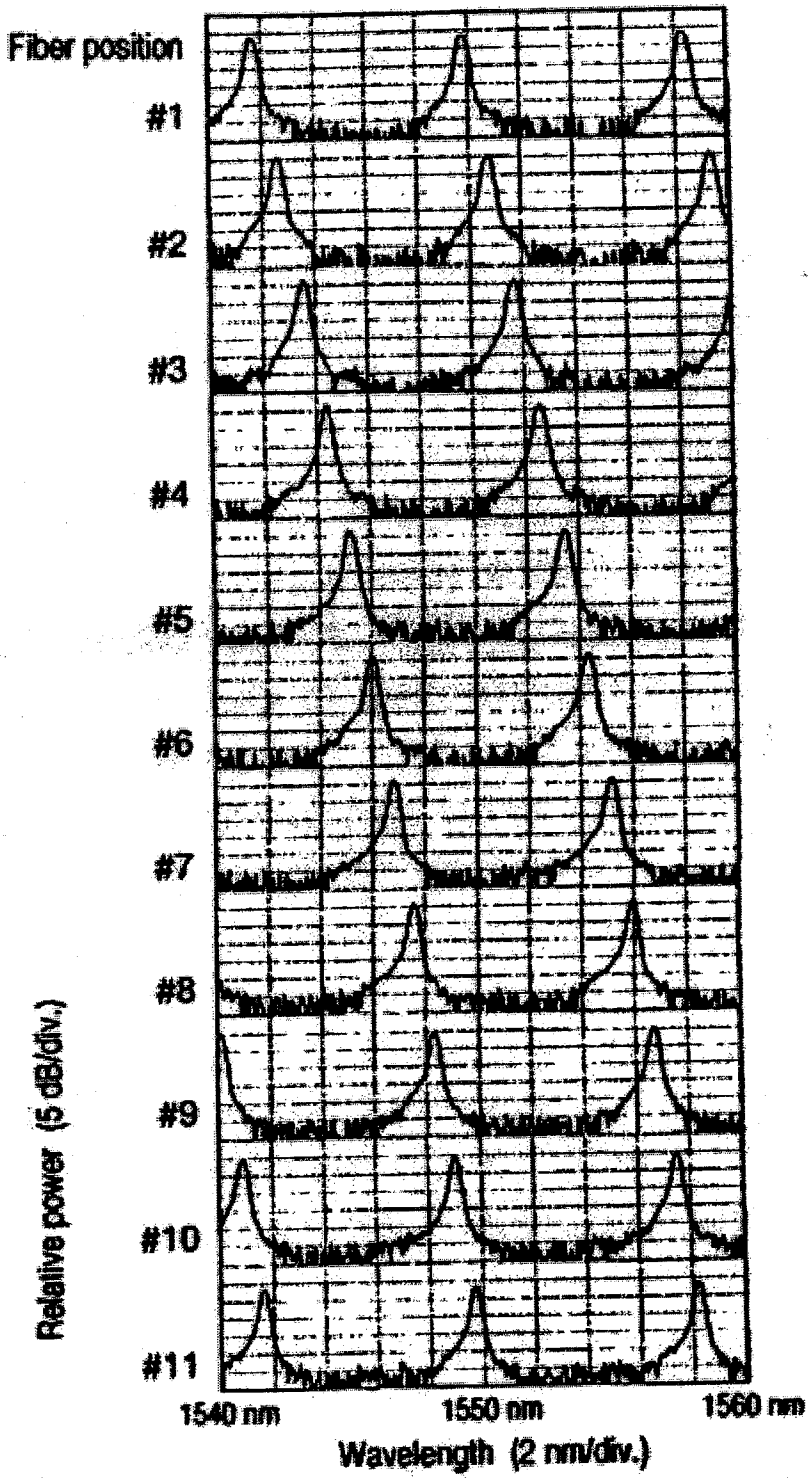

Fig. 1.3. Transmission spectra for the 11 fiber positions. The characteristics for a 10-channel wavelength demultiplexer with 0.8-nm channel spacing are obtained [1].

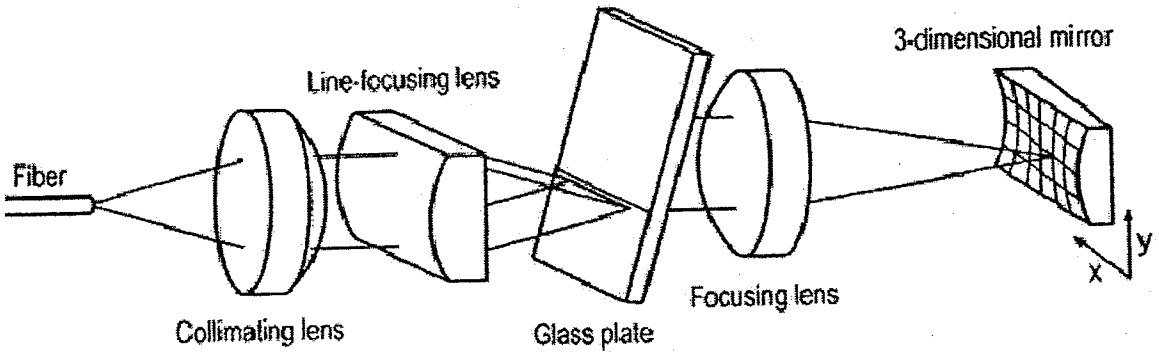

Fig. 1.4. Schematic of the VIPA dispersion compensator. The shorter wavelength travels to the higher position on the mirror, and vice versa. The light is returned from the mirror through the VIPA to the fiber for output [3, 4].

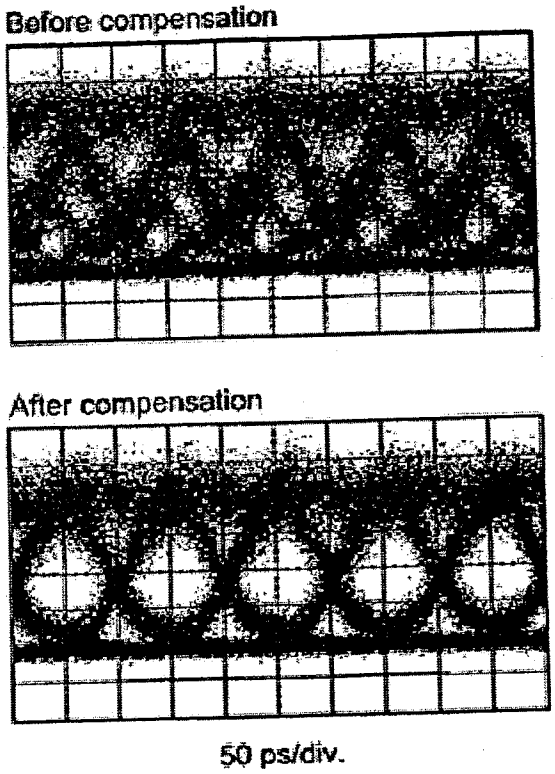

Fig. 1.5. Eye diagrams before and after the dispersion compensation. The eye diagram is clearly recovered through the dispersion compensation. Both are measured with 10-Gb/s nonreturn-to-zero (NRZ) signals at 1.55-um after 110-km transmission of a standard single mode fiber (SMF) [3].

2. GAUSSIAN BEAM AND LENS TRANSFORM

2.1 Introduction

In this section, the equivalence between the paraxial wave equation and the Fresnel scalar diffraction integral is clearly verified and proved. We believe this to be a most complete verification of this equivalence. Specially, H. A. Haus mentioned briefly the idea of this equivalence without any detailed derivation [11]. The other references [10, 12, 13, 14] only focus on one of the two wave theories without discussion of the other one. The derivation of the Optical Fourier Transform (OFT) [10, 11, 12] is repeated here. The OFT only deals with the transform between the front focal plane and the back focal plane. Further more, an extension of the OFT, a general lens transform, which deals with the transform between an arbitrary input plane and output plane, is given with a complete derivation. This result will be used in the following chapters. Useful results from the general lens transform were previously used by our group member D. E. Leaird in DST pulse shaper theory for analysis of chirp control in time domain [15, 16, 17]. However, our discussion will focus on spatial domain analysis. Since the lens transform is derived from Fresnel scalar diffraction theory, it is valid to apply the transform to the Gaussian beam solutions from the paraxial wave equation. The expressions made in this chapter will be the starting point for the analysis of VIPA behavior of the later chapters.

2.2 Paraxial Wave Equations

The phase convention $\exp(i\omega t - i\vec{k} \bullet \vec{r})$ is used in this thesis.

The well-known wave propagation equation is the Helmhotz equation for sinusoidal solutions $\hat{E}(x,y,z)\exp(i\omega t)$ of the Maxwell equation

$$(\nabla^2 + k^2)\hat{E}(x,y,z) = 0 \tag{2.1}$$

Where ∇^2 is the Laplace operator defined as $\frac{\partial^2}{\partial x^2} + \frac{\partial^2}{\partial y^2} + \frac{\partial^2}{\partial z^2}$

For waves propagating in z direction, we can write the field as

$$\hat{E}(x,y,z) = \tilde{E}(x,y,z)\exp(-ikz)$$

Now, inserting the above expression into (2.1), and simplifying, we have

$$(\frac{\partial^2}{\partial x^2} + \frac{\partial^2}{\partial y^2} + \frac{\partial^2}{\partial z^2} - 2ik\frac{\partial}{\partial z})\tilde{E}(x,y,z) = 0 \tag{2.2}$$

Now, we use the paraxial approximation: the second order partial derivative with respect to z is much smaller than the other partial derivative terms.

$$(\frac{\partial^2}{\partial x^2} + \frac{\partial^2}{\partial y^2} - 2ik\frac{\partial}{\partial z})\tilde{E}(x,y,z) = 0 \tag{2.3}$$

Equation (2.3) is called the paraxial wave equation [11, 12, 13, 14], and it is the central wave equation in laser theory for Gaussian beams. The lowest order $TEM_{0,0}$ mode solution is

$$\hat{E}(x,y,z) = E_0 \frac{w_0}{w(z)}\exp\left[-\frac{x^2+y^2}{w^2(z)}\right]\exp\left\{-i\left[kz - \tan^{-1}\left(\frac{z}{z_o}\right)\right]\right\}\exp\left[-i\frac{k(x^2+y^2)}{2R(z)}\right] \tag{2.4}$$

With $w^2(z), R(z), and\ z_o$ given by

$$w^2(z) = w_0^{\,2}\left[1+\left(\frac{z}{z_o}\right)^2\right],\quad R(z) = z\left[1+\left(\frac{z_o}{z}\right)^2\right],\quad z_o = \frac{\pi w_0^{\,2}}{\lambda_0}$$

If there is a much smaller variation in y compared to that in x, we can write the 1-D Gaussian beam as

$$\hat{E}(x,z)=E_0\sqrt{\frac{w_0}{w(z)}}\exp\left[-\frac{x^2}{w^2(z)}\right]\exp\left\{-i\left[kz-\frac{1}{2}\tan^{-1}\left(\frac{z}{z_o}\right)\right]\right\}\exp\left[-i\frac{kx^2}{2R(z)}\right] \quad (2.5)$$

For the case of cylindrical lens focusing with a well collimated beam with a large beam size as input, the expression for the laser field after the lens is given by

$$\hat{E}(x,y,z)=E_0\sqrt{\frac{w_0}{w(z)}}\exp\left[-\frac{x^2}{w^2(z)}\right]\exp\left[-\frac{y^2}{W^2}\right]\exp\left\{-i\left[kz-\frac{1}{2}\tan^{-1}\left(\frac{z}{z_o}\right)\right]\right\}\exp\left[-i\frac{kx^2}{2R(z)}\right] \quad (2.6)$$

W is the radius of the collimated beam, w_0 is the beam waist of the focused beam.

There are also higher order TEM solutions. In usual situations, the lowest order TEM mode is enough to describe laser beams in free space. For simplicity, we do not consider higher order solutions here.

2.3 Scalar Diffraction Theory

Starting from the Helmholtz equation, we suppose the wave vector is inclined by a small angle with respect to z, and use the Fresnel paraxial approximation:

$$k_z=\sqrt{k^2-k_x^{\,2}-k_y^{\,2}}\approx k-\frac{k_x^{\,2}+k_y^{\,2}}{2k} \quad (2.7)$$

Or, equivalently in x-y-z space

$$r=\sqrt{(x-x')^2+(y-y')^2+z^2}\approx z+\frac{(x-x')^2}{2z}+\frac{(y-y')^2}{2z} \quad (2.8)$$

We can obtain the Fresnel diffraction integral [7, 8, 9]

$$\tilde{E}_o(x,y)=\frac{i}{\lambda z}\iint\tilde{E}_i(x',y')\exp\left[-ik\frac{(x-x')^2}{2z}\right]\exp\left[-ik\frac{(y-y')^2}{2z}\right]dx'dy' \quad (2.9)$$

Define the Fresnel kernel as

$$h(x,y,z)=\frac{i}{\lambda z}\exp\left[-ik\frac{x^2+y^2}{2z}\right] \quad (2.10)$$

Then, the field in the object plane is just the convolution of the field from the source

plane with the Fresnel kernel

$$\tilde{E}_o(x,y,z) = \tilde{E}_i(x,y) * h(x,y,z)$$

(Note: for simplicity, we do not carry along explicitly the phase factor $\exp(-ikz)$ as in Gaussian wave equations.)

Now, we need to verify one important result: the equivalence between the Fresnel diffraction integral and the Gaussian wave equation. This means the Fresnel diffraction integral is an exact solution of the paraxial wave equation, and we must obtain the same field profile as the analytic Gaussian beam solution by the Fresnel diffraction. Instead of direct verification of (2.9), we can insert Fresnel kernel (2.10) into the paraxial wave equation to verify the important equivalence of these two solutions.

By direct derivative, we can have following relations:

$$-2ik\frac{\partial}{\partial z}h = -2ik\left(-\frac{1}{z} + ik\frac{x^2+y^2}{2z^2}\right)h = \left(2i\frac{k}{z} + k^2\frac{x^2+y^2}{z^2}\right)h \tag{2.11}$$

$$\frac{\partial^2}{\partial x^2}h = \left(-k^2\frac{x^2}{z^2} - i\frac{k}{z}\right)h \tag{2.12}$$

$$\frac{\partial^2}{\partial y^2}h = \left(-k^2\frac{y^2}{z^2} - i\frac{k}{z}\right)h \tag{2.13}$$

By inserting (2.11) - (2.13) into the paraxial wave equation (2.3), we can easily finish the verification:

$$\left(\frac{\partial^2}{\partial x^2} + \frac{\partial^2}{\partial y^2} - 2ik\frac{\partial}{\partial z}\right)h = \left(-k^2\frac{x^2}{z^2} - i\frac{k}{z}\right)h + \left(-k^2\frac{y^2}{z^2} - i\frac{k}{z}\right)h + \left(2i\frac{k}{z} + k^2\frac{x^2+y^2}{z^2}\right)h = 0$$

So, the Fresnel diffraction integral is the solution of the paraxial wave equation.

Now, we study Fraunhofer diffraction, which is the limit of Fresnel diffraction for the large distance between the source plane at z=0 and the object plane at z. The approximation is the far-field limit for the source, which means

$$\frac{k}{z}\left[(x-x')^2 + (y-y')^2\right] \approx \frac{k}{z}\left[(x^2+y^2) - 2xx' - 2yy'\right] \tag{2.14}$$

The term $\frac{k}{z}(x'^2+y'^2)$ is ignored. Thus, Fresnel diffraction goes to Fraunhofer diffraction

$$\tilde{E}_o(x,y,z)=\frac{i}{\lambda z}\exp\left[-i\frac{k}{2z}\left[x^2+y^2\right]\right]\iint\tilde{E}_i(x',y')\exp\left(\frac{ikxx'+ikyy'}{z}\right)dx'dy'$$

(2.15)

A result of diffraction theory applied to a thin lens system is the OFT: the front focal plane and the back focal plane are exactly a Fourier transform pair, i.e., the field profile of back focal plane is exactly the Fourier transform of the field profile in the front focal plane. The OFT is a direct result of Fresnel diffraction applied to this lens system without the far-field approximation. The full analytic expression of the OFT is

$$\tilde{E}_o(x,y)=\frac{i}{\lambda F}\iint\tilde{E}_i(x',y')\exp\left(\frac{ikxx'+ikyy'}{F}\right)dx'dy' \qquad (2.16)$$

Please note that the OFT is different from the Fraunhofer diffraction integral; however, a special case of Fraunhofer diffraction reduces to the OFT, which is a far-field limit for the object, i.e., we ignore the quadratic phase factor outside of the integral in (2.15).

We will derive (2.16) in section 2.4.

2.4 Derivation of Optical Fourier Transform (OFT)

Basically, there are two ways to derive the OFT in the lens system: the Transfer Function and Direct Diffraction Integration. Both Goodman and Haus use the transfer function, and Ramo uses the direct diffraction integration. The following derivation follows that of Ramo [7, 8, 9].

$\tilde{E}_i(x,y),\tilde{E}_1(x,y),\tilde{E}_2(x,y)$ and $\tilde{E}_o(x,y)$ are the field distributions on the plane with a distance d to the left side of thin lens, the plane exactly before the thin lens, the plane exactly after the thin lens and the back focal plane, respectively. The thin lens has a focal

length of F.

According to the thin lens phase transfer function, we have the key relation

$$\tilde{E}_2(x',y') = \tilde{E}_1(x',y')\exp(ik\frac{x'^2+y'^2}{2F}) \tag{2.17}$$

According to the Fresnel diffraction integral (2.9)

$$\tilde{E}_o(x,y) = \frac{i}{\lambda F}\iint \tilde{E}_2(x',y')\exp\left[-ik\frac{(x-x')^2}{2F}\right]\exp\left[-ik\frac{(y-y')^2}{2F}\right]dx'dy' \tag{2.18}$$

Inserting (2.17) into (2.18), we get

$$\tilde{E}_o(x,y) = \frac{i}{\lambda F}\exp(-ik\frac{x^2+y^2}{2F})\iint \tilde{E}_1(x',y')\exp\left[ik\frac{xx'}{F}\right]\exp\left[ik\frac{yy'}{F}\right]dx'dy' \tag{2.19}$$

By using the Fresnel diffraction integral, we have the relation between $\tilde{E}_i$ and $\tilde{E}_1$

$$\tilde{E}_1(x',y') = \frac{i}{\lambda d}\iint \tilde{E}_i(x_i,y_i)\exp\left[-ik\frac{(x_i-x')^2}{2d}\right]\exp\left[-ik\frac{(y_i-y')^2}{2d}\right]dx_i dy_i \tag{2.20}$$

Note: $\int_{-\infty}^{\infty}\exp(iax^2+ibx)dx = \sqrt{\frac{i\pi}{a}}\exp(-i\frac{b^2}{4a})$

$$\int_{-\infty}^{\infty}\exp(-ik\frac{x'^2}{2d})\exp\left[ik(\frac{x_i}{d}+\frac{x}{F})\right]x'dx' = \sqrt{\frac{i\pi}{-k/2d}}\exp\left[i\frac{kd}{2}(\frac{x_i}{d}+\frac{x}{F})^2\right] \tag{2.21}$$

$$\int_{-\infty}^{\infty}\exp(-ik\frac{y'^2}{2d})\exp\left[ik(\frac{y_i}{d}+\frac{y}{F})\right]y'dy' = \sqrt{\frac{i\pi}{-k/2d}}\exp\left[i\frac{kd}{2}(\frac{y_i}{d}+\frac{y}{F})^2\right] \tag{2.22}$$

Inserting (2.20) into (2.19), using integrals (2.21) and (2.22), then (2.19) becomes

$$\tilde{E}_o(x,y) = \frac{i}{\lambda F}\exp\left[-i\frac{k}{2F}(1-\frac{d}{F})(x^2+y^2)\right]\iint \tilde{E}_i(x',y')\exp(\frac{ikxx'+ikyy'}{F})dx'dy' \tag{2.23}$$

Note, we just change the subscript of x_i and y_i to x' and y' respectively for convenience.

If d=F, i.e., we choose the front focal plane as the input, we can simplify (2.23) to

$$\tilde{E}_o(x,y) = \frac{i}{\lambda F}\iint \tilde{E}_i(x',y')\exp\left(\frac{ikxx'+ikyy'}{F}\right)dx'dy' \tag{2.24}$$

(2.24) is the exact Optical Fourier Transform between input field on the front focal plane and output field on the back focal plane.

2.5 General Lens Transform

Finally, we would like to derive a general expression for the thin lens system. Instead of setting the receiving plane at the back focal plane, let's see the general transform formula for a field at the plane with a distance d_1 to the left side of lens and the field at the plane with a distance d_2 to the right side of lens. Assume all regions are in the Fresnel region. Following the same derivation as for the OFT, we can obtain the following important conclusions:

Let $q = \frac{1}{F} - \frac{1}{d_1} - \frac{1}{d_2}$

If $q = 0$, in fact, this is the geometric optics imaging system, and the transform is

$$\begin{aligned}
&\tilde{E}_o(x,y) = -\frac{1}{d_1 d_2}\exp(-ik\frac{x^2+y^2}{2d_2})\times \\
&\iint \tilde{E}_i(x',y')\exp\left[-ik\frac{x'^2}{2d_1}\right]\exp\left[-ik\frac{y'^2}{2d_1}\right]\delta(\frac{x'}{d_1}+\frac{x}{d_2})\delta(\frac{y'}{d_1}+\frac{y}{d_2})dx'dy' \qquad (2.25)\\
&= -\tilde{E}_i(-\frac{d_1}{d_2}x,-\frac{d_1}{d_2}y)\exp\left[-ik\frac{d_1+d_2}{2d_2^{\,2}}\left(x^2+y^2\right)\right]
\end{aligned}$$

The δ function indicates

$$\frac{x'}{d_1}+\frac{x}{d_2} = \frac{y'}{d_1}+\frac{y}{d_2} = 0 \qquad (2.26)$$

This is exactly the geometric optics image formula, which yields the geometric relations between object and image.

If $q \neq 0$, the transform is

$$\tilde{E}_o(x,y)=\frac{-i}{\lambda d_1 d_2 q}\times\exp\left[-i\frac{k}{2}\left(\frac{x^2}{qd_2{}^2}+\frac{x^2}{d_2}\right)\right]\exp\left[-i\frac{k}{2}\left(\frac{y^2}{qd_2{}^2}+\frac{y^2}{d_2}\right)\right]\times$$
$$\iint\tilde{E}_i(x',y')\exp\left[-i\frac{k}{2}\left(\frac{x'^2}{qd_1{}^2}+\frac{x'^2}{d_1}\right)\right]\exp\left[-i\frac{k}{2}\left(\frac{y'^2}{qd_1{}^2}+\frac{y'^2}{d_1}\right)\right]\exp\left(-i\frac{kx'x+ky'y}{qd_1d_2}\right)dx'dy' \tag{2.27}$$

We define some terms:

F-F: the lens transform for $d_1=F,d_2=F$

NF-F: the lens transform for $d_1\neq F,d_2=F$

F-NF: the lens transform for $d_1=F,d_2\neq F$

NF-NF: the lens transform for $d_1\neq F,d_2\neq F$

Here are some important discussions

For $d_1=d_2=F$, so $q=-\frac{1}{F}$, F-F, (2.27) reduces to the OFT (2.24);

For $d_1=d\neq F,d_2=F$, so $q=-\frac{1}{d}$, NF-F, (2.27) reduces to (2.23);

For $d_1=F,d_2=d\neq F$, so $q=-\frac{1}{d}$, F-NF, (2.27) reduces to (2.28)

$$\tilde{E}_o(x,y)=\frac{i}{\lambda F}\times$$
$$\iint\tilde{E}_i(x',y')\exp\left[-i\frac{kx'^2}{2F}\left(1-\frac{d}{F}\right)\right]\exp\left[-i\frac{ky'^2}{2F}\left(1-\frac{d}{F}\right)\right]\exp\left(i\frac{kx'x+ky'y}{F}\right)dx'dy' \tag{2.28}$$

In real OFT image systems, there may be a small deviation of the input and output field planes from the front and back focal plane; (2.27) can be used to compute the resulting error. One point that must be emphasized is that (2.23) and (2.28) demonstrate the different functions of the z displacements of the input and output planes from the corresponding focal planes. In the usual case where the intensity distribution is of interest, a z displacement of the input plane doesn't change the intensity distribution, but a z displacement of the output plane must change the intensity distribution. The point is that (2.23) has quadratic phase terms only outside of the integral, but (2.28) has the

quadratic phase terms inside of the integral. So the z-position of output plane is a very sensitive parameter, and we must make it as close as possible to the focal position to avoid unwanted effects. Another special term used to mean this intensity distribution is power spectrum, which is measured directly with a spectrum analyzer. The power spectrum discussed here is similar to that for signals in time. For the VIPA spectral disperser, the power spectrum means the diffraction intensity distribution for a certain wavelength on the back focal plane.

2.6 Discussion

We have identified the equivalence between Fresnel diffraction theory and the paraxial wave equation. We also identify, in F-F thin lens systems, that the Optical Fourier Transform is a direct result of Fresnel diffraction theory. As a Gaussian beam is a solution of the paraxial wave equation, we can use the OFT for the Gaussian beam transform in the F-F lens systems. The only requirement is the validity of the paraxial approximation. It is very convenient to apply the OFT for the Gaussian beam transform in the F-F lens systems, and all amplitude and phase information is included in the OFT for Gaussian beams.

We also generalize the transform to the lens systems: NF-F, F-NF, NF-NF. NF-F yields a Fourier transform with additional quadratic phase; F-NF and NF-NF yield a complex non Fourier transform of the input. A special case in NF-NF is the geometric optics imaging, which must be dealt with separately. We also find out that NF-F doesn't change the power spectrum, but F-NF and NF-NF will change the power spectrum. In optical spectrometer systems, the output plane must be carefully set as close to the back focal plane as possible to obtain the correct power spectrum.

3. VIPA DEMULTIPLEXER SPECTRUM AND SPATIAL CHIRP EFFECT

3.1 VIPA Demultiplexer Theory Model

The incident beam is assumed to be a Gaussian beam [Fig. 3.2]. This is reasonable since the incident beam into the VIPA is a collimated beam focused by a cylindrical lens. All virtual sources have the same spatial Gaussian profile with an exponentially decreasing intensity. From the incident beam spot, an index 0, 1, 2... is assigned to these Gaussian beam sources. The spatial profile of n^{th} virtual source can be written as

$$E_0 (Rr)^n \exp\left[-\frac{(x - n2t\sin\theta_i)^2}{w_0^{\,2}} \right] \tag{3.1}$$

R, r are the field reflectivity on the highly and partially reflective surfaces. The thickness of VIPA etalon is t. w_0 is the incident beam waist size. θ_i is the incident angle.

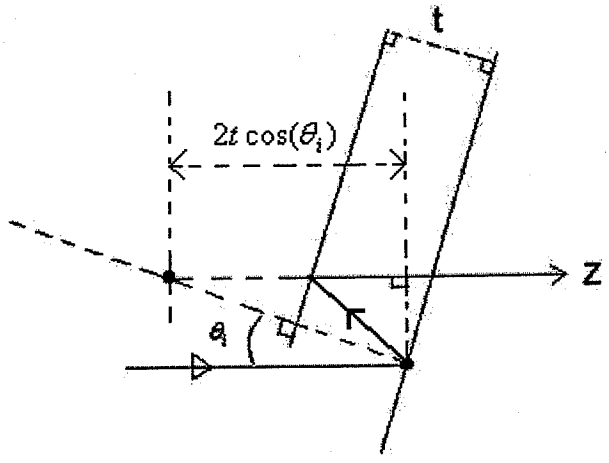

Fig. 3.1. The trigonometry for the virtual sources. The sources have a transverse space $2t\sin(\theta_i)$, and the longitudinal space for neighboring sources is $2t\cos(\theta_i)$

The incident beam axis is assumed to match the optical axis of the thin lens, and the incident beam spot on the transmission side is in the front focal plane of the thin lens. According to the geometrical relations in fig. 3.1., the n^{th} source has a longitudinal (optical axis) distance to the thin lens

$$d_{1_n} = F + n2t\cos\theta_i \tag{3.2}$$

If the VIPA has a physical width L, the total number of sources is ~ $L/[2t\tan(\theta_i)]$.

The fiber receiver is placed in the back confocal region of the thin lens, where the wavelengths are dispersed due to the spectral dispersion of the VIPA. The distance between the receiver and the thin lens is d_2.

3.2 Theory For The VIPA Demultiplexer Spectrum Line-Shape

Now, the general lens transform can be applied to this VIPA model to calculate the output field on the receiver plane perpendicular to the optical axis. Obviously, this VIPA model is a NF-NF system.

Recall the general lens transform

$$E_{out}(x_F, y_F) = \frac{-i}{\lambda d_1 d_2 q} \times \exp\left[-i\frac{k}{2d_2}\left(\frac{1}{qd_2}+1\right)({x_F}^2 + {y_F}^2)\right]$$
$$\iint E_{in}(x,y)\exp\left[-i\frac{k}{2d_1}\left(\frac{1}{qd_1}+1\right)(x^2+y^2)\right]\exp\left(-i\frac{kx_F x + ky_F y}{qd_1 d_2}\right)dxdy$$

and $q = \frac{1}{F} - \frac{1}{d_1} - \frac{1}{d_2}$

Please notice the general transform reduces exactly to a spatial Fourier transform when we have $d_1 = d_2 = F$, which means the source plane and object plane match with the front focal plane and back focal plane, respectively.

In our experiment, a well collimated laser source with a beam radius around 1.2 mm (focal depth ~ several meters) is focused into the VIPA by a cylindrical lens. A one

dimensional analysis is enough here, and we can use the 1-D transform instead of the 2-D.

The general NF-NF transform can be reduced to the following useful expression

$$E_{out}(x_F, y_F) = \frac{\tilde{C}}{\lambda d_1 d_2 q} \times \exp\left[-i\frac{k}{2d_2}\left(\frac{1}{qd_2}+1\right)x_F{}^2\right] \int E_{in}(x,y)\exp\left[-i\frac{k}{2d_1}\left(\frac{1}{qd_1}+1\right)x^2\right]\exp\left(-i\frac{kx_F x}{qd_1 d_2}\right)dx \tag{3.3}$$

Recall a useful formula for Fourier transform of Gaussian profile

$$\int \exp\left[-a(x-\Delta)^2\right]\exp(-ibx^2)\exp(-ik'x)dx = \exp(-ib\Delta^2)\exp(-ik'\Delta)\sqrt{\frac{\pi}{a+ib}}\exp\left[-\frac{(a-ib)(k'+2b\Delta)^2}{4(a^2+b^2)}\right] \tag{3.4}$$

For the VIPA demultiplexer model discussed here:

$a = \frac{1}{w_0{}^2}, b = \frac{k}{2d_1}\left(1+\frac{1}{qd_1}\right) = \frac{k}{2}\frac{d_2 - F}{d_1 d_2 - d_1 F - d_2 F}, \Delta = 2nt\sin(\theta_i),\ k' = \frac{kx_F}{qd_1 d_2}$. The incident beam waist is determined by $w_0 = \frac{f\lambda}{\pi W}$, where f is the focal length of the cylindrical lens, W is the collimated beam radius, and λ is the wavelength.

According to the expression for b, b is very sensitive to d_2 and weakly dependent on d_1. The important point is that if there is a slight z deviation of the receiver from the focal plane, it causes obvious additional quadratic phase variation.

Please notice that the most important modification is the first quadratic phase $\exp(-ib\Delta^2)$.

The transform is applied to all the beam sources individually, and then we do a linear summation of all the output field profiles to obtain the total output field.

In order to reduce the computation, some numerical analysis is necessary.

We take typical parameters: F~250mm, W=1.2mm, λ~1.55um, $f \le 300$mm. The VIPA has a width L ~ 10mm, which yields an approximate typical confocal depth

$F - 3mm \le d_2 \le F + 3mm$ determined by $\pi(\lambda F/L)^2/\lambda = \pi\lambda(F/L)^2 \sim 3mm$.

The VIPA we tested has a thickness of 1.5 mm (FSR~100GHz), and the effective beam round trip number is ~20 (The intensity decays to around 1/e after 20 round trips for power reflectivity per trip ~95%), so we have $F \le d_1 \le F + 100mm$. The typical incident angle satisfies $\theta_i \le 15^0$. Finally, we can estimate the range of the important parameters: $b \le 0.1mm^{-2}$ and $a \ge 100mm^{-2}$, so a >>b is a good model. If $x_F = 0$ (the origin), (3.4) reduces to

$$\int \exp\left[-a(x-\Delta)^2\right]\exp(-ibx^2)\exp(-ik'x)dx \approx \sqrt{\frac{\pi}{a}}\exp(-ib\Delta^2)\exp(-ik'\Delta) \qquad (3.5)$$

It is also reasonable to ignore the output field amplitude variation with different sources, i.e. $d_1 d_2 q \approx -F$ is valid for all sources.

With the discussion above, for the nth source, we can write the corresponding output field at the origin ($x_F = 0 \rightarrow k' = 0$)

$$\frac{\tilde{C}}{\lambda F}\sqrt{\pi}w_0(Rr)^n \exp\left[-ikn2t\cos(\theta_i)\right]\exp(-ib\Delta^2) \text{ with } \Delta = 2nt\sin(\theta_i) \qquad (3.6)$$

Thus, the total output field at the origin is

$$E_{out}(x_F = 0, \lambda) \propto \sum_n (Rr)^n \exp\left[-ikn2t\cos(\theta_i)\right]\exp\left[-ib4n^2t^2\sin^2(\theta_i)\right] \qquad (3.7)$$

and $b = \frac{k}{2d_1}(1+\frac{1}{qd_1}) = \frac{k}{2}\frac{d_2 - F}{d_1 d_2 - d_1 F - d_2 F}$

(3.7) is the central equation that determines the VIPA demultiplexer transmission spectrum [18].

The final point to note is that we are focusing on the paraxial region, which is the only region with measurable power in the receiving plane. For the spectral line-shape, we may ignore the spatial dependence of the line-shape, i.e. just look at the output spectral line-shape at the origin of the receiving plane. In fact, as we will see later in this part, the line-shape at the origin is enough to characterize the symmetry behavior of the VIPA demultiplexer spectrum line-shape.

If there is no quadratic phase term in the summation, the transmission spectrum has a similar expression to that of a Fabry-Perot interferometer which has an Airy or Lorentzian line-shape. As we will see later, the quadratic phase in the summation contributes to the spatial chirp effect, i.e., different parts of the VIPA correspond to different center frequencies or wavelengths in the demultiplexing process. The sign of b will decide the direction of line-shape asymmetry and the sign of the spatial chirp. Both the following experiments and theoretical simulations show that positive b (d_2<F) causes a tail to the left, and negative b (d_2>F) causes a tail to the right (Assume the spectra are plotted as functions of wavelength).

3.3 Experiments And Theoretical Simulation

3.3.1 The VIPA demultiplexer spectrum

In the experimental setup (Fig. 3.3), an amplified spontaneous emission laser source (ASE) is used as the input, and the bandwidth is approximately 50 nm from 1520 nm to 1570 nm. The collimated beam has a radius of 1.2 mm, and the incident beam waist is about 24 μm after a cylindrical lens of focal length f = 60mm. An optical spectrum analyzer is used to record the spectrum with attention on the line-shape, and the finest resolution 0.01 nm is used. The VIPA is air filled with a 1.5 mm thickness corresponding to 100 GHz free spectral range. The VIPA etalon has an effective width of about 7mm, and the incident beam leaks out the etalon of finite width L (~10mm) after a certain number of round trip reflections (Since the beam is expanding during its propagation toward the thin lens, the beam spots at the end of VIPA etalon will pass through the edge side of the thin lens in this setup. In order to reduce the lens's aberration, we use a razor blade to cut off these beams spots about 3 mm away from the far end side of the VIPA etalon. This is critical for large incident angles $\geq 10^{o}$. That is why the effective width of 7mm is less than the actual VIPA width (10 mm)).

Fig. 3.4 shows the data from both the experiment and theoretical simulation. The incident angle is fixed at 10 degrees in all cases. The focal length of the thin lens F is ~ 180 mm. Fig. 3.5 shows another set of data for the VIPA with another thin lens of F ~ 250 mm. For the same deviation of the distance d_2 from F (d_2-F fixed), spectra difference occurs for thin lens with different F, and this is clearly demonstrated in Fig. 3.4 and Fig. 3.5. The reason is that the parameter b in (3.17) is different for different F with d_2-F fixed, or the focal depth varies with the F.

We mark the receiver longitudinal position d_2 = F when we obtain the symmetric line-shape experimentally, and then we translate the receiver longitudinally to other positions with respect to the reference position of d_2 = F. If $d_2 \neq F$, the spectral line-shape is asymmetric and broadened compared to that in the case of d_2 = F. As discussed previously, the asymmetry direction depends on the sign of b ($d_2 > F \rightarrow b > 0$; $d_2 < F \rightarrow b < 0$). All line-shapes demonstrate sinc-like behavior with ripples or side peaks. The reason is that the VIPA has a finite width, which indicates that there is a finite number of interfering beam spots. For an infinite number of interfering beam spots and a symmetric line-shape, an Airy or Lorentzian spectrum with a smooth line-shape can be obtained.

One important parameter for a demultiplexer spectrum is the full width at half maximum (FWHM) or 3 dB width.

In the case of a symmetric demultiplexer line-shape, we have the spectrum

$$E_{out}(x_F = 0, \lambda) \propto \sum (Rr)^n \exp[-ikn2t\cos(\theta_i)] \tag{3.8}$$

In the limit of a large number interfering beams, the theoretical minimal FWHM in wavelength is given by

$$FWHM = \frac{\lambda_0^{\,2}}{2\pi t\cos(\theta_i)} \frac{1-Rr}{\sqrt{Rr}} \tag{3.9}$$

A numerical example: wavelength λ_0 ~ 1550 nm, reflectivity Rr ~ 95%, thickness t ~ 1.5 mm, small incident angle $\cos(\theta_i) \sim 1$, $FWHM$ ~ 0.01 nm.

However, the actual FWHM for the VIPA demultiplexer is a little larger than the theoretical limit since there is a finite number of interfering beams ($L/[2t\tan(\theta_i)]$). The experimental FWHM for an incident angle of 10° is ~ 0.05 nm; the FWHM for an incident angle of 5° is ~ 0.02nm (Fig. 3.6). The FWHM for 5° is quite close to the theoretical limit since there is a large number (~30) of interfering beams. The theoretical simulation also yields the same scale value. The larger the number of interfering beams, the narrower the FWHM. By the way, we also tried testing the VIPA under smaller incident angles ~ 2°, where .01 nm FWHM is obtained, but it is not convincing as .01 nm is the minimum resolution of the OSA. The fitting of the reflectivity Rr is feasible if we can measure such a small FWHM with a higher resolution OSA.

3.3.2 Spatial chirp effect

The asymmetric line-shape is also observed in previously published data (Fig. 1.3) as well as in the work of A. Vega [8, 9].

In order to study the asymmetry, we introduce a spatial gate to look at the spectral contributions from different sets of multiple beam spots (local demultiplexing). The setup allows us to have a closer look at how the spectral asymmetry occurs (Fig. 3.7). This method of introducing a spatial gate has also been used in DST pulse shaper experiments in our group [15, 16, 17].

Fig. 3.8 shows the gated VIPA demultiplexer spectrum in a xyz plot. An air-spaced VIPA is used, and the VIPA has the same effective width ~ 7mm. The cylindrical lens has a focal length of 60mm. The thin lens has a focal length of 180 mm. The beam incident angle is ~ 10°. A 3mm wide spatial gate is translated along the VIPA transmission side at a step size of 1mm, and the gated spectrum is recorded by the optical spectrum analyzer (OSA) for each translation step. The y-axis marked with 0,1,2,3,4 is the gate position or gate step. It is obvious that different beam sets of the VIPA contribute to slightly different

demultiplexing wavelengths, and the demultiplexing wavelength shift is demonstrated both in experiments and in theoretical simulation. The total wavelength shift for an incident angle of 10° is ~ 0.05nm according to our data. We call such a demultiplexing wavelength shift the spatial chirp effect for the VIPA. Another interesting point is that we can tune the spatial chirp effect both in amplitude and in sign or direction. This is shown in our data for different values of d_2. d_2<F causes asymmetry with a tail to the left, and d_2>F causes asymmetry with a tail to the right [18].

We also can do a theoretical analysis to see the variation of the local demultiplexing wavelength. To simplify our discussion, Young's double slit interference is used as the theoretical model. Let's recall the demultiplexer equation

$$E_{out}(x_F = 0, \lambda) \propto \sum_n (Rr)^n \exp[-ikn2t\cos(\theta_i)]\exp\left[-ib4n^2t^2\sin^2(\theta_i)\right]$$

The constructive interference phase matching condition for the n^{th} and $n+1^{th}$ beam spot is

$$k2t\cos(\theta_i) + 4b\left[(n+1)^2 - n^2\right]t^2\sin^2(\theta_i) = k2t\cos(\theta_i) + 4b(2n+1)t^2\sin^2(\theta_i) = 2m\pi$$

$$\text{Where, } b = \frac{k}{2}\frac{d_2 - F}{d_1 d_2 - d_1 F - d_2 F} \approx \frac{k}{2}\frac{F - d_2}{F^2} \tag{3.10}$$

From the phase matching condition (3.10), we can obtain the local demultiplexing wavelength (the wavelength of constructive interference)

$$\lambda = \lambda_0\left[1 + \frac{(F - d_2)t\sin^2(\theta_i)}{F^2\cos(\theta_i)}(2n+1)\right], \text{ where, } 2t\cos(\theta_i) = m\lambda_0 \tag{3.11}$$

According to (3.11), the local demultiplexing wavelength increases or decreases linearly with the steps of the spatial gate, and the variation trend depends on the position of the receiver: increasing for d_2 < F; decreasing for d_2 > F; vanishing for d_2 = F. For given d_2-F in our experiments, the approximate total wavelength shift ($\propto \sin(\theta_i)$) for an incident angle of 10° is ~ 0.05nm from (3.11), which matches well with the experimental data. The picture is improved if the spatial gate can exactly select two beam spots during the translation as in Young's double slit interference experiment. In order to have a good

signal to noise ratio (SNR) in our experiment, a spatial gate with width of 3 mm is used, which normally selects more than two beam spots. This is enough to see the approximate linear variation of local constructive wavelength depending on gate position. A point to be noticed is that the total wavelength shift ($\propto \sin(\theta_i)$) increases as the incident angle increases, and that's why we test the spatial chirp effect under a large incident angle ~ 10°.

To have a closer and clearer view of the demultiplexer spectral asymmetry, the gated spectrum (Fig. 3.8) is plotted with the original un-gated spectrum (Fig. 3.9), and we can see how the spatial chirp effect causes the asymmetry. The incident angle is still ~ 10°. The exponential decay of intensity for these beam spots is also a key factor leading to spectral asymmetry together with the spatial chirp effect. The spectrum will be broadened symmetrically if there is only the spatial chirp and constant intensity distribution.

The asymmetrically broadened demultiplexer spectrum is not desired; however, we demonstrate a way to tune the spatial chirp to obtain symmetric line-shape both in theory and experiment (Fig. 3.10). According to our demultiplexer theory, the key parameter for the spatial chirp effect, b, can be adjusted by the receiver's longitudinal position d_2. When d_2 is equal to F, the focal length of the thin lens, b vanishes to zero, and there is no spatial chirp. This is shown in fig. 3.9, where all beam sets contribute to the same demultiplexing wavelength, which makes a compact symmetric line-shape.

To summarize this chapter, we have explained the symmetry behavior of the VIPA demultiplexer spectrum line-shape: the spectral symmetry or asymmetry strongly depends on the receiver's longitudinal position. We identify a spatial chirp effect strongly related to the line-shape asymmetry. Our results are fully explained by our theory.

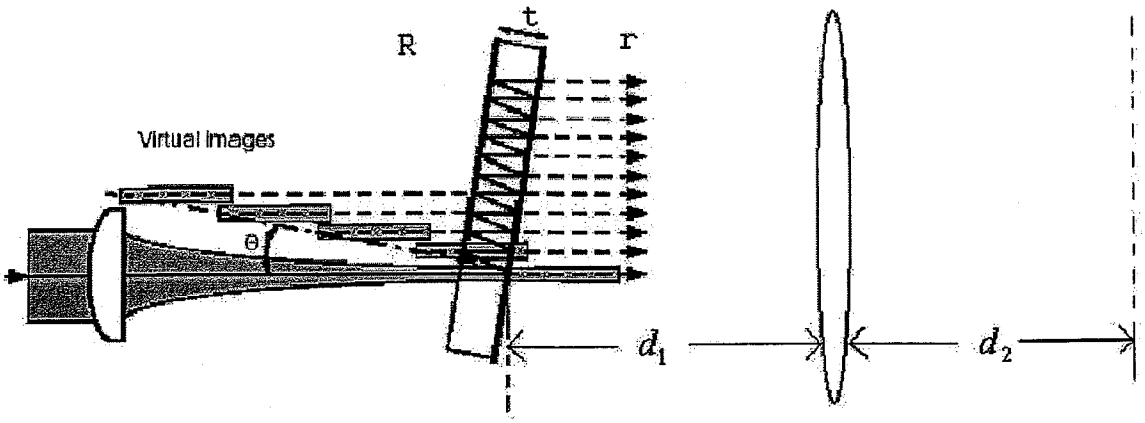

Fig. 3.2. VIPA demultiplexer schematic theory model

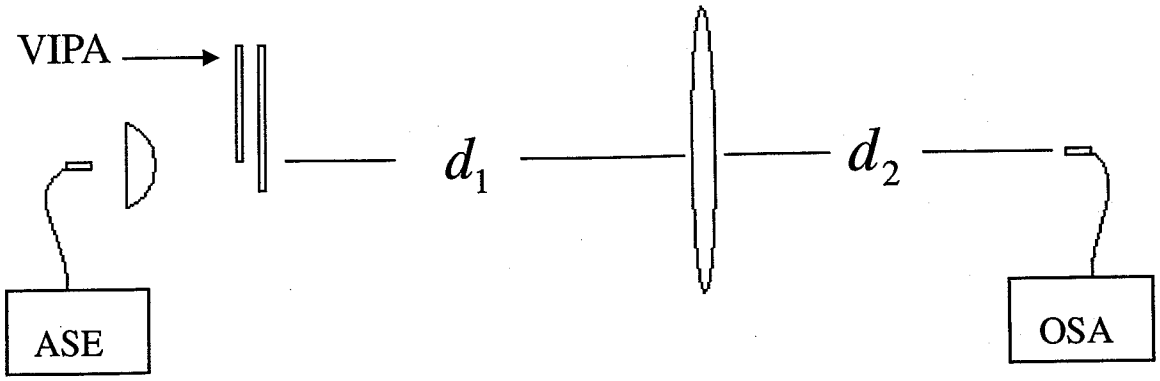

Fig. 3.3. TheVIPA demultiplexer setup. ASE: Amplified Spontaneous Emission, OSA: Optical Spectrum Analyzer. The OSA resolution is set at 0.01 nm.

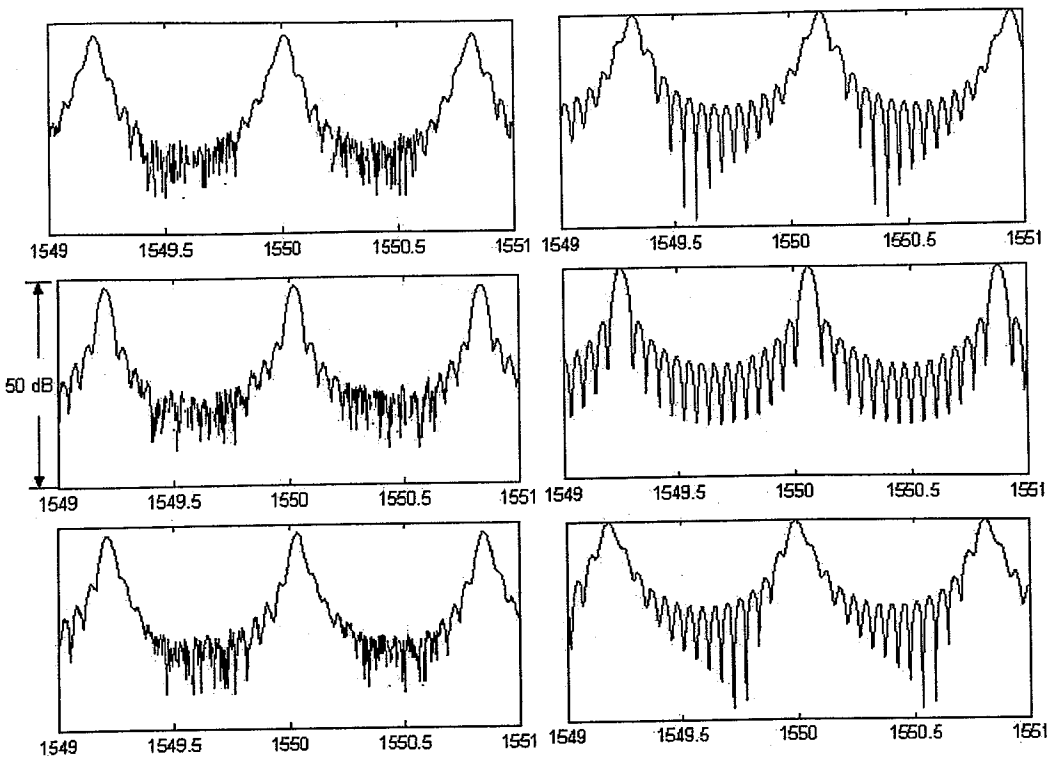

Fig. 3.4. VIPA demultiplexer transmission spectra 1. The left column is experimental data; the right column is data from our theoretical simulation. The 1st row: d_2 = F -2mm; the 2nd row: d_2 = F; the 3rd row: d_2 = F +2mm. F is 180mm. The incident angle is 10°.

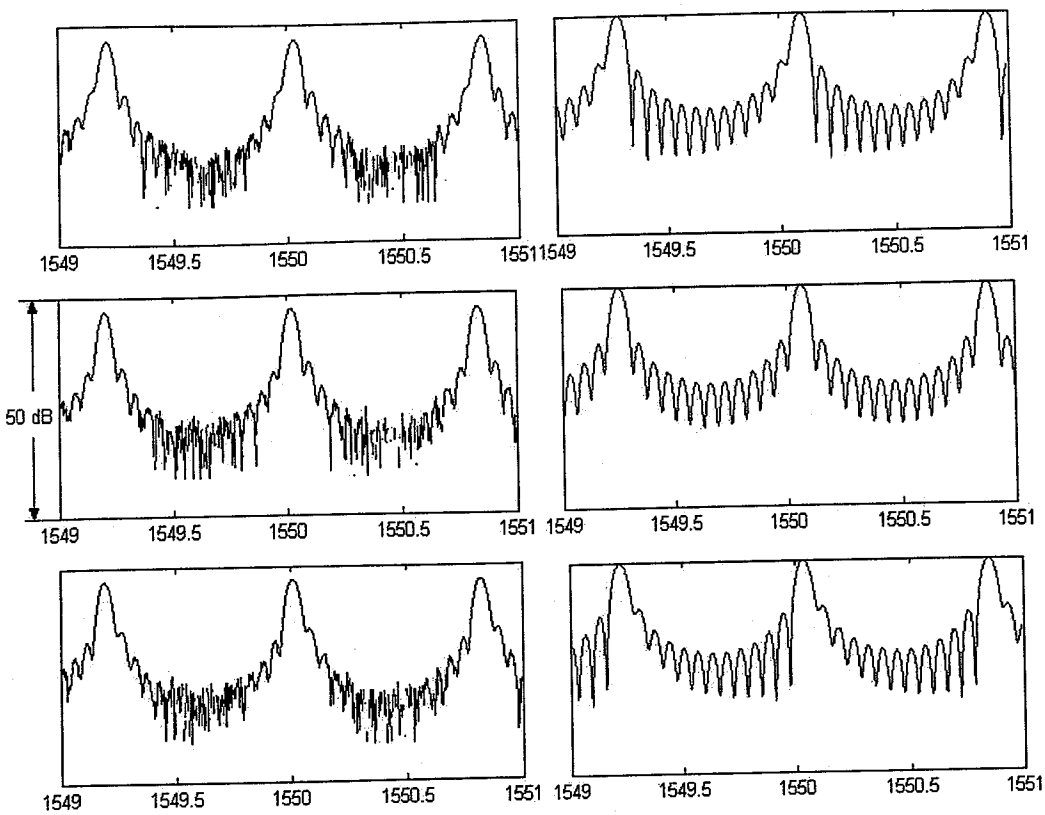

Fig. 3.5. VIPA demultipelxer transmission spectra 2. All plots are arranged in the same order as Fig. 3.4. The same VIPA and the same incident angle are used. Another thin lens with longer focal length F = 250 mm is used.

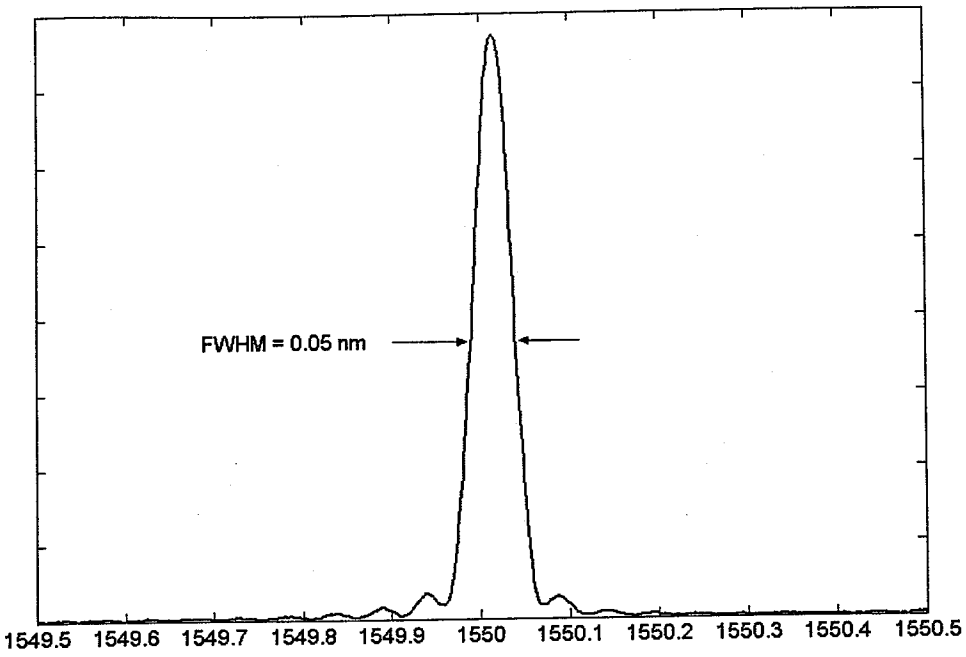

(a)

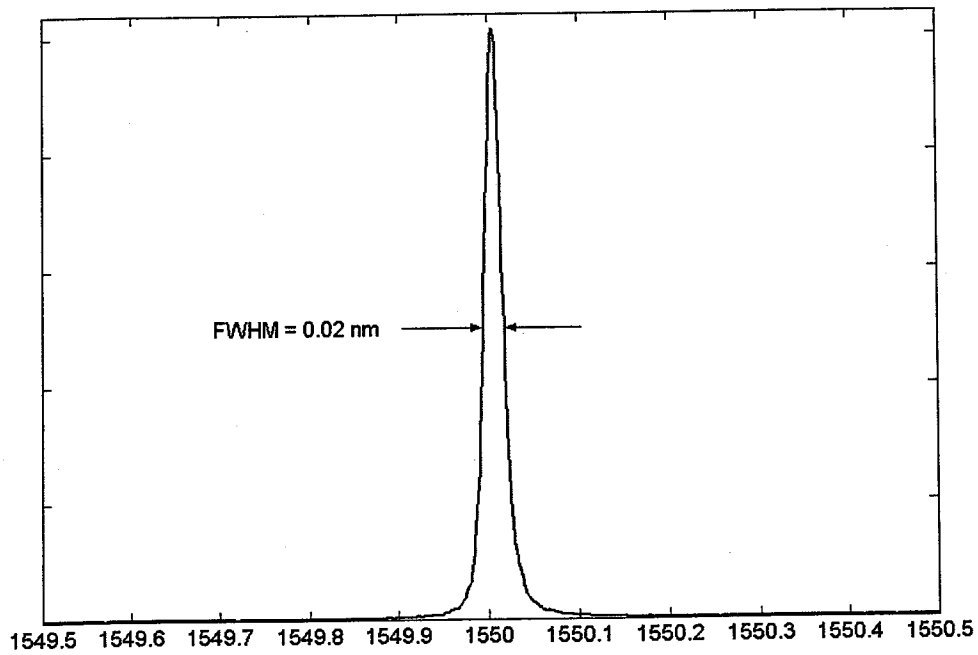

(b)

Fig. 3.6. The symmetric VIPA demultiplexer spectral line-shapes in linear plot. The FWHM is also demonstrated. (a) is for an incident angle ~ 10^{o}; (b) is for an incident angle ~ 5^{o}.

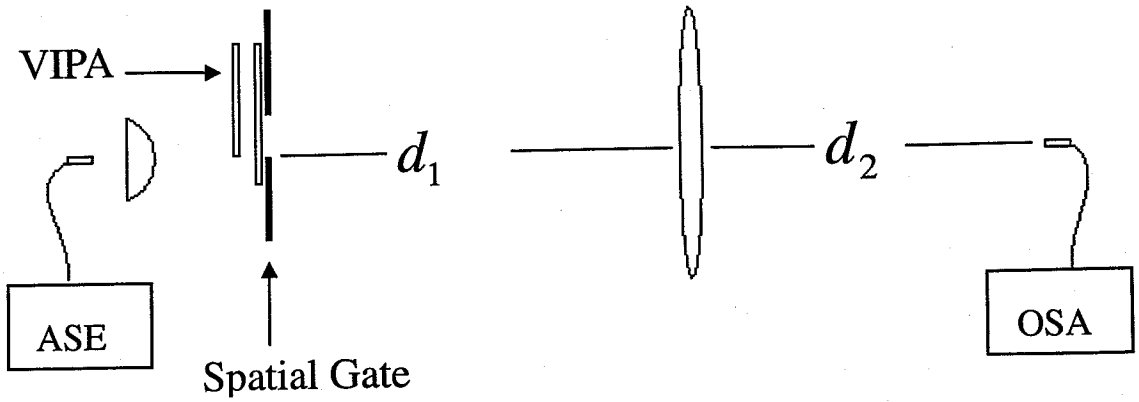

Fig. 3.7. The VIPA with a spatial gate. The gate is translated along the VIPA transmission surface.

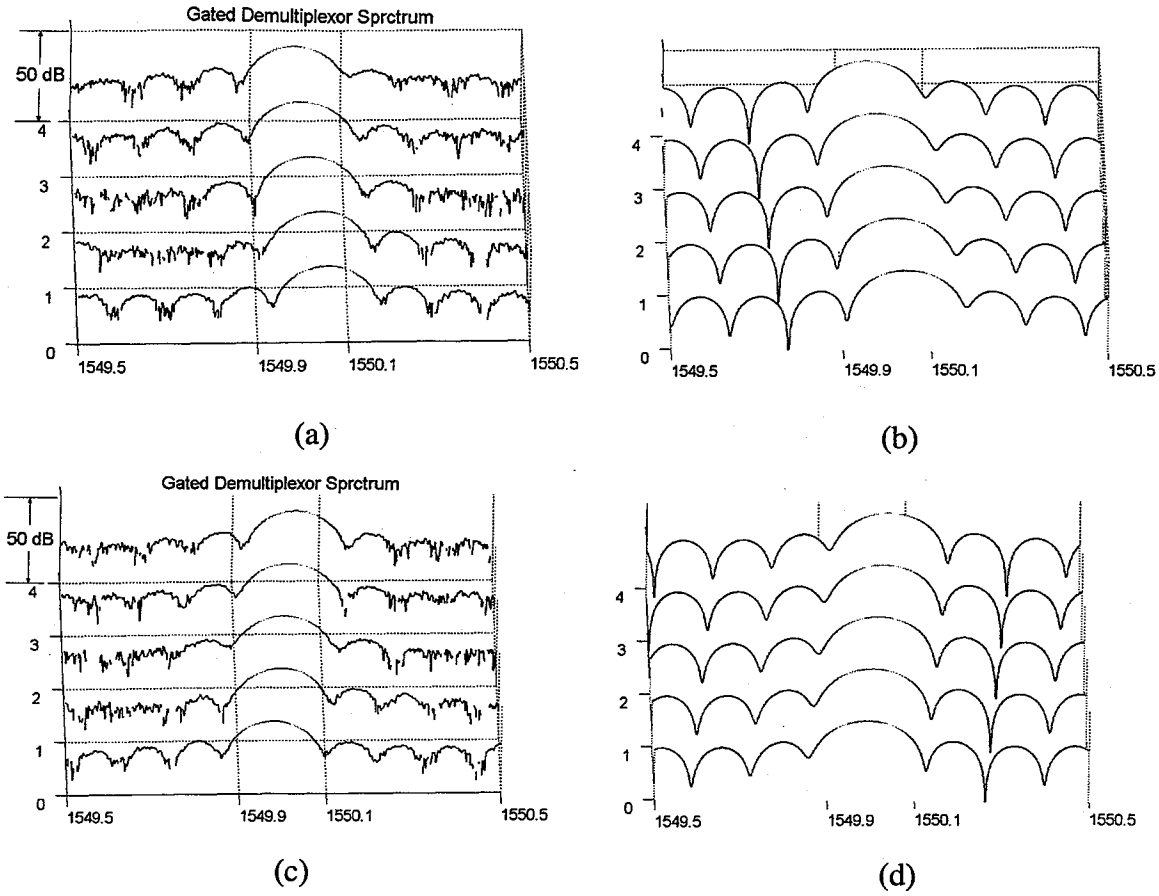

Fig. 3.8. VIPA demultiplexer transmission spectra with a spatial gate. The left column (a) and (c) show experimental data; the right column (b) and (d) are data from our theoretical simulation. d_2 = F+2mm in (a) and (b); d_2= F-2 mm in (c) and (d). The incident angle is 10^o, and the thin lens' focal length F = 180 mm.

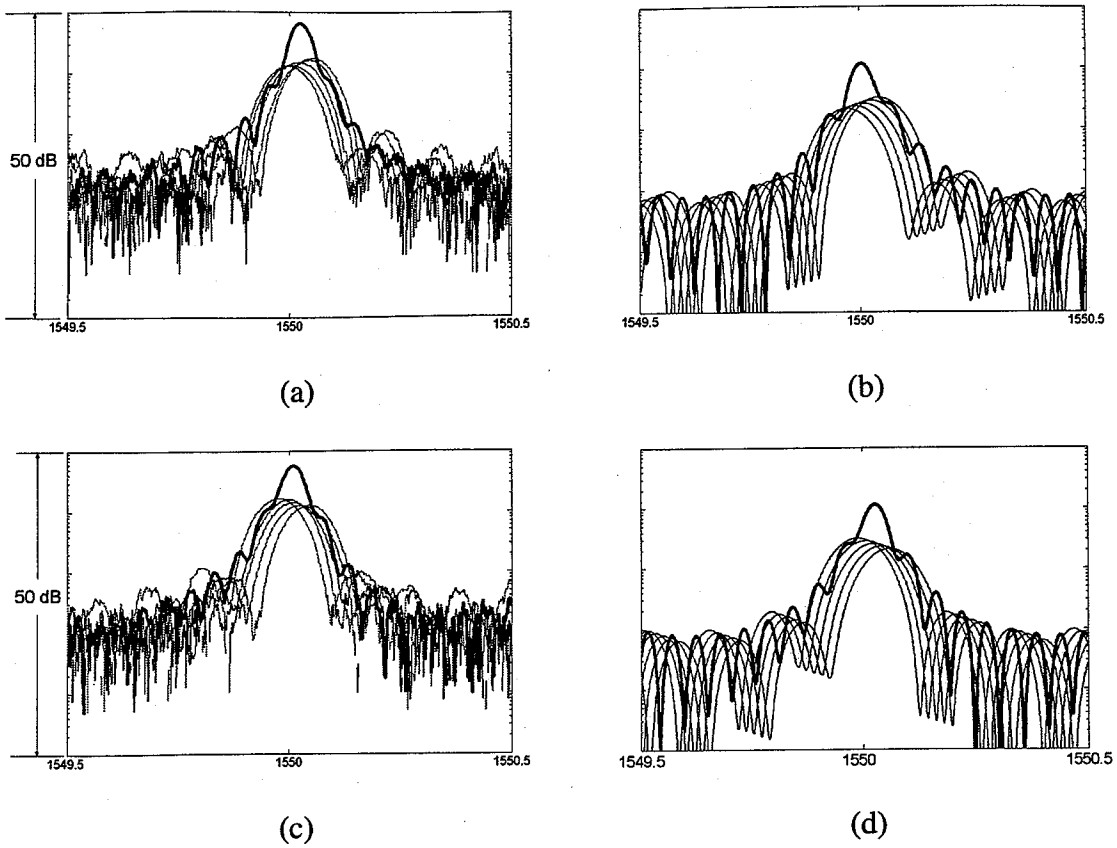

Fig. 3.9. VIPA demultiplexer spectral asymmetry and spatial chirp effect. The left column (a) and (c) are experimental data; the right column (b) and (d) are data from our theoretical simulation. d_2 = F+2mm in (a) and (b); d_2 = F-2mm in (c) and (d). The incident angle is 10^{o}, and the thin lens's F = 180 mm.

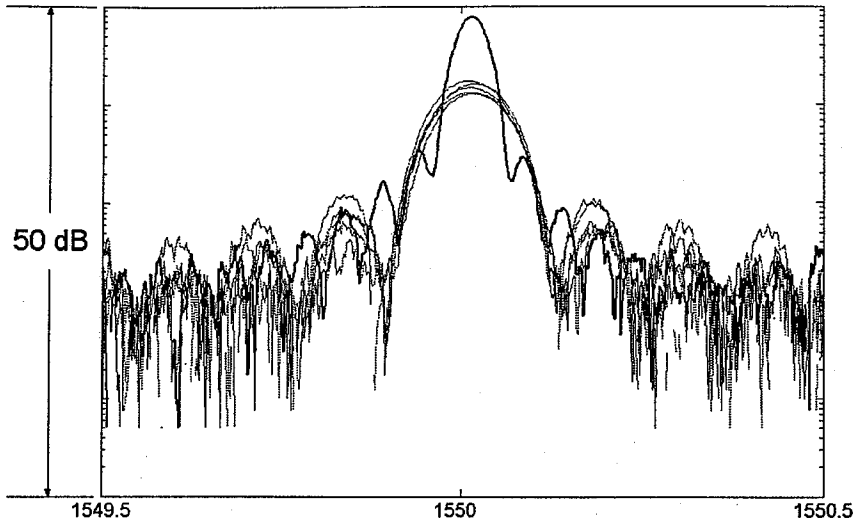

(a)

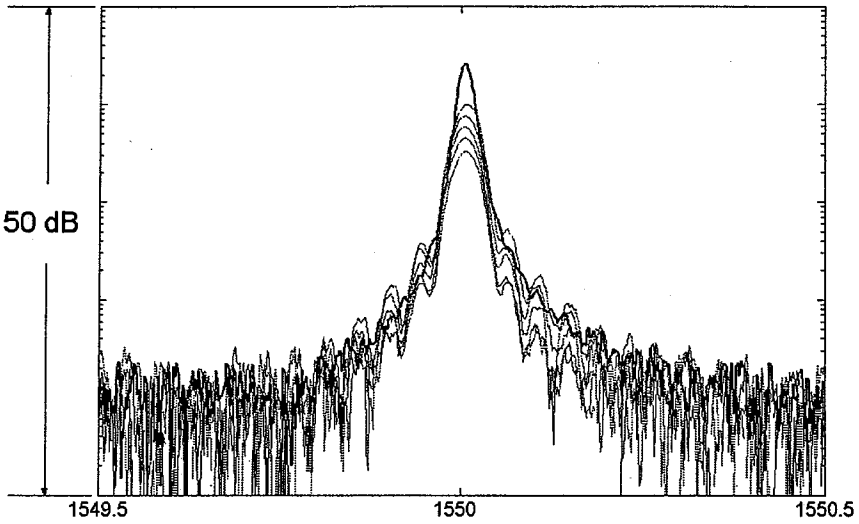

(b)

Fig. 3.10. Experimental symmetric demultiplexer spectrum and spectrum with the spatial gate. (a) is for an incident angle ~ 10^{o}; (b) is for an incident angle ~ 5^{o}.

4. VIPA DISPERSION LAW

4.1 Introduction

In the case of the spatial chirp-free VIPA spectral disperser, it is interesting and meaningful to discuss the dispersion law of the VIPA. This means the receiver's longitudinal position is exactly at the back focal plane of the thin lens, and the general lens transform will reduce to a spatial Fourier transform (for F-F or NF-F lens system). There have been several publications related to dispersion relations of the VIPA. The earliest one is by M. Shirasaki [1], but he only mentioned simple, approximate expressions for the factor of angular dispersion without any detailed derivation; A. Vega formally proposed a dispersion law by plane wave theory [8, 9], and he mainly focused on the free spectral range (FSR). To the best of our knowledge, we present the first complete theoretical analysis and experimental verification of the dispersion relation for wavelength vs. output angle.

4.2 Basic Theory

We use the phase convention $\exp(i\omega t - ikz)$ for a forward propagating wave. We do not explicitly carry the k•z phase term in our following derivation.

An incident Gaussian beam bounces back and forth inside the VIPA etalon until it escapes due to the finite length of the etalon. Because of the partial reflection of the etalon transmission surface, the ray bouncing inside shows an exponentially decaying intensity or energy. Finally, multiple discrete Gaussian beam spots are formed on the

etalon transmission surface. The centers of all the spots are equally spaced according to the mirror reflection. Instead of the virtual sources in chapter 3, we will derive the dispersion relations via the expanding Gaussian beam spot formulation described in this paragraph. We will demonstrate the equivalence later in this section.

The field distribution on the back focal plane is the spatial Fourier Transform of the field on the front focal plane. But the VIPA is tilted, which means all spots are not on the same object plane perpendicular to the optical axis of the thin lens, so the total input field and the output field are not exactly a Fourier pair. In this case, we need to use the NF-F lens transform. Since the input field is the linear sum of multiple spots, we can calculate the transform for each of them, and then sum all the transforms to obtain the total output field distribution.

Assuming the incident spot is at the incident beam waist, we may express the mask function of the VIPA as follows:

$$E_{in_n}(x,\lambda) = E_0\sqrt{\frac{w_0}{w_n}}\exp\left(-\frac{(x-\Delta x_n)^2}{w_n^{\,2}}\right)\exp(-\frac{y^2}{W^2})\exp\left(-i\frac{\pi x^2}{R_n\lambda}\right)\exp(i\phi_n) \qquad (4.1)$$

$n = 0,1,2,3.....$, 1-D Gaussian beam. $\Delta x_n = 2nt\sin(\theta_i)$.

The n is the index of all spots from the incident spot to the last spot on the transmission side. The square root of the beam waist ratio is a factor for power conservation along the x distribution that we are interested in. W is the radius of the collimated beam. R_n is the phase curvature for the nth beam spot on the transmission surface. w_n is the beam waist of the nth beam spot on the transmission surface.

The total field at the VIPA transmission surface is (the transmission coefficient is included in E_0)

$$E_{in}(x,\lambda) = \sum_{n=0}^{N}(Rr)^n E_{in_n}(x,\lambda) \qquad (4.2)$$

R, r are the reflection coefficients of the VIPA's highly reflective and transmission surface erespectively.

$$\phi_n = \left[-kz_n + \frac{1}{2}\tan^{-1}\left(\frac{z_n}{z_o}\right)\right]_{Gaussian} = -\frac{4\pi nt}{\lambda\cos(\theta_i)} + \frac{1}{2}\tan^{-1}\left(\frac{2nt}{z_o\cos(\theta_i)}\right)$$

$$\phi_{diffraction} = k2nt\tan(\theta_i)\sin(\theta_i) = 4\pi nt\tan(\theta_i)\sin(\theta_i)/\lambda$$

$$\Phi_n = \phi_n + \phi_{diffraction} = -\frac{4\pi t\cos(\theta_i)}{\lambda} + \frac{1}{2}\tan\left(\frac{2nt}{z_o\cos(\theta_i)}\right) \tag{4.3}$$

$$z_o = \frac{\pi w_0^{\,2}}{\lambda},\ z_n = 2nt/\cos(\theta_i),\ w_0 = \frac{f\lambda}{\pi W} \tag{4.4}$$

$$w_n^{\,2} = w_0^{\,2}\left(1+\frac{z_n^{\,2}}{z_o^{\,2}}\right),\ R_n = z_n + \frac{z_o^{\,2}}{z_n},\ z_o = \frac{\pi w_0^{\,2}}{\lambda} \tag{4.5}$$

Where, W is the radius of the collimated beam, is assumed to be independent of wavelength around the 1.55 um range. The f is the focal length of the cylindrical lens.

The phase of the Gaussian beam corresponds to the geometrical optical path AB+BC shown in fig. 4.1, which includes the k•z phase and the arc-tangential phase. The k•z phase of the diffraction integral corresponds to the path AD shown in fig. 4.1. A, C are the centers of two neighboring Gaussian beam spots on the transmission side.

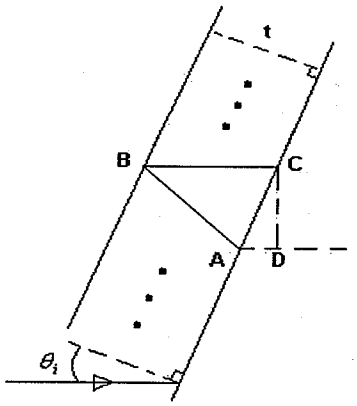

Fig. 4.1 Optical path in the VIPA

Noticing the Fourier Transform of a general Gaussian function:

$$\int_{-\infty}^{\infty}\exp\left[-(a+ib)t^2\right]\exp(i\omega t)dt = \sqrt{\frac{\pi}{a+ib}}\exp\left[\frac{-(a-ib)\omega^2}{4(a^2+b^2)}\right]$$

$$\int_{-\infty}^{\infty}\exp\left[-(a+ib)(t-t_0)^2\right]\exp(i\omega t)dt = \sqrt{\frac{\pi}{a+ib}}\exp(i\omega t_0)\exp\left[\frac{-(a-ib)\omega^2}{4(a^2+b^2)}\right] \tag{4.6}$$

Recall the NF-F lens transform

$$\tilde{E}_o(x,y)=\frac{i}{\lambda F}\exp\left[-i\frac{k}{2F}(1-\frac{d}{F})(x^2+y^2)\right]\iint\tilde{E}_i(x',y')\exp(\frac{ikxx'+ikyy'}{F})dx'dy'$$

The output field of the nth beam spot is

$$\begin{aligned}E_{out_n}(x_F,\lambda)&=\frac{iW\sqrt{\pi}}{\lambda F}(Rr)^n\exp(-\frac{W^2k_y{}^2}{4})\\&\times\exp(-in\lambda t\tan(\theta_i)\sin(\theta_i)k_x{}^2/2\pi)\int E_{in_n}(x,\lambda)\exp(ik_xx)dx\\&=E_0\frac{iW\sqrt{\pi}}{\lambda F}(Rr)^n\exp(-\frac{W^2k_y{}^2}{4})\sqrt{\frac{w_0}{w_n}}\sqrt{\frac{\pi}{a_n+ib_n}}\\&\times\exp\left[\frac{-(a_n-ib_n)k_x{}^2}{4(a_n{}^2+b_n{}^2)}\right]\exp(-i\lambda z_n\sin^2(\theta_i)k_x{}^2/4\pi)\exp(i\Phi_n)\end{aligned}\qquad(4.7)$$

Where, $a_n=\frac{1}{w_n{}^2}$, $b_n=\frac{\pi}{R_n\lambda}$, $k_x=\frac{2\pi x_F}{\lambda F}$, $k_y=\frac{2\pi y_F}{\lambda F}$

(k_x, k_y are spatial frequencies in the optical Fourier system. Phases from the Gaussian beam and the diffraction in (4.3) are combined in Φ_n.)

We also have these relations according to the Gaussian beam profile:

It is easy to verify the following equation by using (4.5)

$$\frac{a_n}{a_n{}^2+b_n{}^2}=w_0{}^2,\frac{b_n}{a_n{}^2+b_n{}^2}=w_0{}^2\frac{z_n}{z_o},\frac{b_n}{a_n}=\frac{z_n}{z_o},a_n{}^2+b_n{}^2=\frac{1}{w_0{}^2w_n{}^2}\qquad(4.8)$$

The amplitude of (4.7) is:

$$\left|E_{out_n}(x_F,\lambda)\right|=E_0\frac{f}{F}\exp(-\frac{W^2\pi^2y_F{}^2}{\lambda^2F^2})\exp\left(-\frac{f^2}{F^2}\frac{x_F{}^2}{W^2}\right)\qquad(4.9)$$

Note, (4.9) can be checked with (4.1) for total power or energy conservation over the beam cross section.

Notice the amplitude is a Gaussian function of the spatial coordinate in the back focal plane, and it is independent of the spots index (n). Each beam spot has the same intensity output profile but a different phase profile. The phase of (4.6) is

$$\exp(i\phi_n)\exp(i\frac{\pi}{2})\exp\left[-\frac{i}{2}\tan^{-1}(z_n/z_o)\right]\exp(ik_x\Delta x_n)\exp\left(\frac{iz_n\cos^2(\theta_i)w_0{}^2k_x{}^2}{4z_o}\right)=$$

$$\exp(i\frac{\pi}{2})\exp\left(-i\frac{4n\pi t\cos(\theta_i)}{\lambda}\right)\exp(i\frac{4n\pi t\sin(\theta_i)x_F}{\lambda F})\exp\left(\frac{i2n\pi t\cos(\theta_i)x_F{}^2}{\lambda F^2}\right)$$

(4.10)

Note, the quadratic phase of the input results in a 1/2 nonlinear arc-tangential phase too, but this arc tangential phase counteracts that resulting directly from the Gaussian beam. Now, we can write the optical lens transform of (4.2)

$$E_{out}(x_F,\lambda)=E_0\frac{f}{F}\exp(-\frac{W^2\pi^2y_F{}^2}{\lambda^2F^2})\exp\left(-\frac{f^2}{F^2}\frac{x_F{}^2}{W^2}\right)\exp(i\frac{\pi}{2})$$

$$\sum_{n=0}^{N}\left\{(Rr)^n\exp\left(-i\frac{4n\pi t\cos(\theta_i)}{\lambda}\right)\exp\left(i\frac{2n\pi t\cos(\theta_i)x_F{}^2}{\lambda F^2}\right)\exp\left(i\frac{4n\pi t\sin(\theta_i)x_F}{\lambda F}\right)\right\}$$

(4.11)

To obtain (4.11), we have performed a complex derivation by utilizing the Gaussian beam profile. However, there is a more efficient way to derive (4.11). The key idea is to apply the NF-F lens transform by utilizing the virtual sources of the VIPA. Assuming the incident beam's waist is on the front focal plane, we have a simple spatial profile of input sources. The NF-F transform is used to calculate the output of each individual virtual source. The final output field is the linear sum of all these calculated individual outputs. This way is similar to that of chapter 3, where we take the virtual sources as the input field, not the expanding Gaussian beam spots used above. The equivalence of the two physical pictures of VIPA is demonstrated here.

The beam profile is a non-chirped Gaussian function for each beam source with an exponentially decreasing intensity.

$$E_n(x,y)=(Rr)^nE_0\exp(-\frac{(x-\Delta x_n)^2}{w_0{}^2})\exp(-\frac{y^2}{W^2}) \qquad (4.12)$$

n=0, 1, 2, 3...

The nth source has a z displacement $\Delta z_n = 2nt\cos(\theta_i)$ with respect to the front focal

plane.

The output field at the back focal plane due to the n[th] source is

$$E_{out_n}(x_F, y_F) = \frac{i}{\lambda F}\exp\left[i\frac{k\Delta z_n}{2F^2}(x_F{}^2 + y_F{}^2)\right]\iint E_{in_n}(x,y)\exp(\frac{ikx_F x + iky_F y}{F})dxdy \quad (4.13)$$

The amplitude of each output field is

$$\left|E_{out_n}(x_F, \lambda)\right| = E_0(Rr)^n \frac{f}{F}\exp(-\frac{W^2\pi^2 y_F{}^2}{\lambda^2 F^2})\exp\left(-\frac{f^2}{F^2}\frac{x_F{}^2}{W^2}\right) \quad (4.14)$$

The phase of each output field is

$$\exp(i\frac{\pi}{2})\exp\left(-i\frac{4n\pi t\cos(\theta_i)}{\lambda}\right)\exp(i\frac{4n\pi t\sin(\theta_i)x_F}{\lambda F})\exp\left(\frac{i2n\pi t\cos(\theta_i)x_F{}^2}{\lambda F^2}\right) \quad (4.15)$$

According to (4.14) and (4.15), we have the same amplitude and phase profile that is obtained by using expanding Gaussian beam spots. It is obvious that the use of virtual sources is much faster than using expanding Gaussian beam spots to derive the field on the back focal plane because we can avoid the complex relations of the Gaussian beam.

Since we only measure the power spectrum or intensity distribution on the back focal plane, the distance between the VIPA and lens can be arbitrary within the validity of paraxial approximation (For convenience, we assumed the incident spot is exactly on the front focal plane). The reason is the NF-F and F-F lens systems yield the same power spectrum because their difference is only a phase outside of Fourier integral. This is also verified in experiments.

4.3 VIPA Dispersion Law

If we assume N is large enough (valid for small incident angles) so that we can perform an infinite series sum, the simplified output field is:

$$E_{out}(x_F,\lambda) \propto \exp\left(-\frac{f^2}{F^2}\frac{{x_F}^2}{W^2}\right)\times \frac{1}{1-Rr\exp\left(-i\frac{4\pi t\cos(\theta_i)}{\lambda}+i\frac{4\pi t\sin(\theta_i)x_F}{\lambda F}+\frac{i2\pi t\cos(\theta_i){x_F}^2}{\lambda F^2}\right)} \tag{4.16}$$

The output intensity is:

$$I_{out}(x_F,\lambda) \propto \exp\left(-\frac{2f^2{x_F}^2}{F^2W^2}\right)\frac{1}{(1-Rr)^2+4(Rr)\sin^2\left(\frac{k\Delta}{2}\right)} \tag{4.17}$$

Where, $\Delta = 2t\cos(\theta_i)-\frac{2t\sin(\theta_i)x_F}{F}-\frac{t\cos(\theta_i){x_F}^2}{F^2}$

With a CW input, the output diffraction intensity is an Airy function distribution under a Gaussian window along the x direction on the back focal plane. The VIPA interferometer demonstrates an Airy-Lorentzian line shape similar to the Fabry-Perot interferometer.

The transmission peak wavelengths satisfy the constructive interference condition:

$$k\Delta = k\left[2t\cos(\theta_i)-\frac{2t\sin(\theta_i)x_F}{F}-\frac{t\cos(\theta_i){x_F}^2}{F^2}\right] = 2m\pi \tag{4.18}$$

Under the paraxial approximation $\frac{x_F}{F}\approx\theta_o$ (ignore third or higher orders of the output angle), (4.18) can be written as

$$k\left[2t\cos(\theta_i)-2t\sin(\theta_i)\theta_o-t\cos(\theta_i){\theta_o}^2\right] = 2m\pi \tag{4.19}$$

Equation (4.19) is the dispersion law of the VIPA under the paraxial approximation.

The free spectral range (FSR) is

$$FSR = \frac{c}{2t\cos(\theta_i)-2t\sin(\theta_i)\theta_o-t\cos(\theta_i){\theta_o}^2} \tag{4.20}$$

In a second order Taylor series, (4.20) can be expanded into the following expression

$$FSR = \frac{c}{2t\cos(\theta_i)}\left\{1+\tan(\theta_i)\theta_o + \left[\frac{1}{2}+\tan^2(\theta_i)\right]\theta_o{}^2\right\} \tag{4.21}$$

An important corollary from (4.19) is the dependence of the constructive interfering wavelength on output angle, which is related to the angular dispersion:

$$\Delta\lambda = \lambda - \lambda_0 = -\lambda_0\left[\tan(\theta_i)\theta_o + \frac{1}{2}\theta_o{}^2\right] \quad \text{with } m\lambda_0 = 2t\cos(\theta_i) \tag{4.22}$$

The dependence of the output angle on wavelength is

$$\theta_o = -\tan(\theta_i) + \sqrt{\tan^2(\theta_i) - 2\frac{\lambda-\lambda_0}{\lambda_0}} \tag{4.23}$$

In (4.23), there is also another solution of minus the square root, which is not correct since the output angle decreases as wavelength increases for the fixed order of m [1, 2, 4]. Another direct explanation: λ_0 is defined such that $\theta_o = 0$ at $\lambda = \lambda_0$.

The angular dispersion expression is

$$\frac{d\theta_o}{d\lambda/\lambda_0} = -\frac{1}{\tan(\theta_i)+\theta_o} \tag{4.24}$$

The angular dispersion relation (4.22) can be reduced for large incident angles:

$$\theta_o = -\cot(\theta_i)\frac{\lambda-\lambda_0}{\lambda_0}$$

Equations (4.21) or (4.22) can be checked with experiment directly to verify the VIPA dispersion law (4.19).

Before we proceed to our simulation and experimental data, we would like to recall the Vega-Weiner VIPA dispersion law based on plane wave theory. The Vega-Weiner dispersion law is

$$\omega\frac{2t}{c}\left\{\frac{1}{\cos\theta_i} - \tan(\theta_i)\sin(\theta_i+\theta_o)\right\} = 2m\pi \tag{4.25}$$

Under the paraxial approximation, we can reduce (4.25) to the following expression

$$k\left|2t\cos(\theta_i) - 2t\sin(\theta_i)\theta_o + t\tan(\theta_i)\sin(\theta_i)\theta_o{}^2\right| = 2m\pi \tag{4.26}$$

The FSR under a second order of Taylor series from this dispersion law is

$$FSR = \frac{c}{2t\cos(\theta_i)}\left[1+\tan(\theta_i)\theta_o+\frac{1}{2}\tan^2(\theta_i)\theta_o^{\,2}\right] \tag{4.27}$$

The wavelength vs. output angle relation would be

$$\Delta\lambda = \lambda-\lambda_0 = -\lambda_0\left[\tan(\theta_i)\theta_o-\frac{1}{2}\tan^2(\theta_i)\theta_o^{\,2}\right] \text{ with } m\lambda_0 = 2t\cos(\theta_i) \tag{4.28}$$

The relative ratio of $\Delta\lambda$ by (4.28) vs. (4.22) is written as

$$\gamma = \frac{\tan(\theta_i)\theta_o-\tan^2(\theta_i)\theta_o^{\,2}/2}{\tan(\theta_i)\theta_o+\theta_o^{\,2}/2} = \frac{1-\tan(\theta_i)\tan(\theta_o)/2}{1+\frac{1}{2}\frac{\tan(\theta_o)}{\tan(\theta_i)}} \tag{4.29}$$

Note that the paraxial approximation $\theta_o \approx \tan(\theta_o)$ is used in (4.29).

By comparing (4.19) with (4.26), (4.21) with (4.27) and (4.22) with (4.28), we can see the important difference is the quadratic term of the output angle. (4.29) is used to show the difference vs. incident angles for the two dispersion theories. Theoretical curves are plotted in Fig. 4.2, where the comparison is shown. Our new dispersion theory demonstrates a nontrivial effect of this quadratic term under small incident angles (<5°) with $\gamma \neq 1$, which is trivial in Vega-Weiner theory with opposite sign; and the effect of this quadratic term is trivial under incident angles (>10°) with $\gamma \approx 1$, so the two theories yield the same result for the first order of output angles.

In the region where power can be well measured ($|\theta_o| \leq 1.5^o$ in experiments here), the paraxial approximation is always valid, which means it is meaningful and interesting to do a paraxial theory and to compare with Vega-Weiner theory under the paraxial approximation. According to (4.29) and Fig. 4.2, we need to set the VIPA at small incident angles (<5°) to measure the obvious quadratic relations of (4.19); otherwise, we have an approximate linear relation, which has been confirmed in Vega-Weiner's work [8, 9].

4.4 Experiments and Theory Fitting

Since the case of large incident angle is carefully studied in the Vega-Weiner theory [8, 9], we only focus on small incident angles with a strong second order effect as discussed in our theory.

The experimental setup is almost the same as the demultiplexer setup in Fig. 3.2 except that the fiber receiver is translated transversely along the x-axis on the back focal plane. Various experiments under different conditions are done to test the relation between output angle and wavelength. The dispersion data is plotted in Fig. 4.3 (a), (b), (c), (d). Both theory and experiment demonstrate that the angular dispersion is a function of both the incident angle and the output angle. For a fixed incident angle, the angular dispersion increases as the output angle decreases. The numerical value of the dispersion from our data here is ≥ 1 deg/nm in the operating region we are testing.

According to our angular dispersion law, the angular dispersion is not dependent on the incident beam focusing condition, which is especially demonstrated by Fig. 4.3 (b) and 4.3 (c). Fig. 4.3 (b) is loose focusing with a cylindrical lens (CYL) of 300mm focal length, and Fig. 4.3 (c) is tight focusing with a CYL of 60 mm focal length. The incident beam waist sizes are 120 um and 24 um respectively. Further, theoretical fitting can be applied to calculate some experimental parameters, which are the exact focal length of thin lens and the exact incident angle. Fitting is applied to Fig. 4.3 (b), (c) respectively, and we use formula (4.28) in $\theta_o = x_F / F$. The circles shown in Fig. 4.4 are raw data from experimentation, and the solid line is the theoretical curve. The theoretical curve and the experimental data match quite well. A fixed output angle of zero degrees is fixed for the two fittings. The fitting results are: F=258.9 mm, incident angle = 1.26 degree for Fig. 4.4 (b); F=258.7 mm, incident angle = 1.02 degree for Fig. 4.4 (c). They both yield the same F under possible small error, and this is in good agreement with our dispersion law.

For more convincing theoretical fitting, it is better to maintain a fixed reference for incident angles, and a fixed zero position of the output angle is still taken. The rotation stage has a division of 1 degree. Although the absolute zero incident angle is hard to identify, the relative angle difference can be identified from the rotation stage. We conduct another dispersion testing under incident angles of 0°, 1°, 2°, 3° according to the rotation stage respectively. The same compound thin lens with F = 180 mm is used here. The dispersion data is plotted in (a)-(d) of Fig. 4.5. The theoretical fitting is plotted in (a)-(f) of Fig. 4.6. The average fitting values for the 4 corresponding incident angles are 1.17, 2.07, 3.00, 4.02 degrees, which matches well with the reading from the rotation stage. To compare with the Vega-Weiner dispersion theory, the dispersion curve by Vega-Weiner theory is also plotted together with the fittings. As it is in the previous discussion, the Vega-Weiner dispersion is an approximately linear law in the paraxial region of output, and this is clearly demonstrated in these plots. The difference of the two dispersion laws is also obvious to see. Around the zero degree of output angle, the two theories yield almost the same linear dispersion relation; far away from the zero position of output angle, the Vega-Weiner theory deviates from the actual dispersion that is a quadratic curve described fully by our new theory. As the incident angle is larger, the difference of the two theories becomes smaller in the paraxial region of output angles.

Another necessary fitting is for thickness of the VIPA. In a group of dispersion data for wavelength vs. output angle with the same incident angle, the neighboring quadratic dispersion curves have the two reference wavelengths that satisfy the following equations:

$$m\lambda_{01} = 2t\cos(\theta_i) \tag{4.30}$$

$$(m+1)\lambda_{02} = 2t\cos(\theta_i) \tag{4.31}$$

The combination of (4.30) and (4.31) yields

$$t = \frac{1}{2\cos(\theta_i)} \frac{\lambda_{01}\lambda_{02}}{\lambda_{01} - \lambda_{02}} \tag{4.32}$$

By using a previous fit for these reference wavelengths and the incident angle, we can calculate the thickness of the VIPA (marked 1.5 mm corresponding to 100 GHz FSR). We use the arithmetic average for the incident angle in (4.32) of fitting angles by each dispersion curve under the same incident angle. The calculated thickness from the previous dispersion data under 1°, 2°, 3° incident angles are 1.484 mm, 1.485 mm, 1.486 mm respectively. These calculated thickness values match well with the given standard.

Although our theory and experiment focus on the air-filled VIPA with a 100GHz FSR, it is fully applicable to air-filled VIPA with different FSR, and it is also applicable to the solid VIPA with small modifications with consideration of the effect of the refractive index (n_r) of the etalon. The corresponding key equations for the solid VIPA are

$$k\left[2t\frac{n_r-\sin(\theta_{in})\sin(\theta_i)}{\cos(\theta_{in})}-2t\tan(\theta_{in})\cos(\theta_i)\theta_o-t\frac{n_r-\sin(\theta_{in})\sin(\theta_i)}{\cos(\theta_{in})}\theta_o^{\,2}\right]=2m\pi \quad (4.33)$$

where $n_r\sin(\theta_{in})=\sin(\theta_i)$ (Snell's Law), and θ_{in} is the internal incident angle in the solid etalon.

The relation between wavelength and the output angle is expressed by

$$\Delta\lambda=\lambda-\lambda_0=-\lambda_0\left[\frac{\sin(\theta_{in})\cos(\theta_i)}{n_r-\sin(\theta_{in})\sin(\theta_i)}\theta_o+\frac{1}{2}\theta_o^{\,2}\right] \quad (4.34)$$

where, $m\lambda_0=2t\dfrac{n_r-\sin(\theta_{in})\sin(\theta_i)}{\cos(\theta_{in})}$.

All these equations are reduced to that of the air-spaced VIPA by setting the refractive index $n_r=1$.

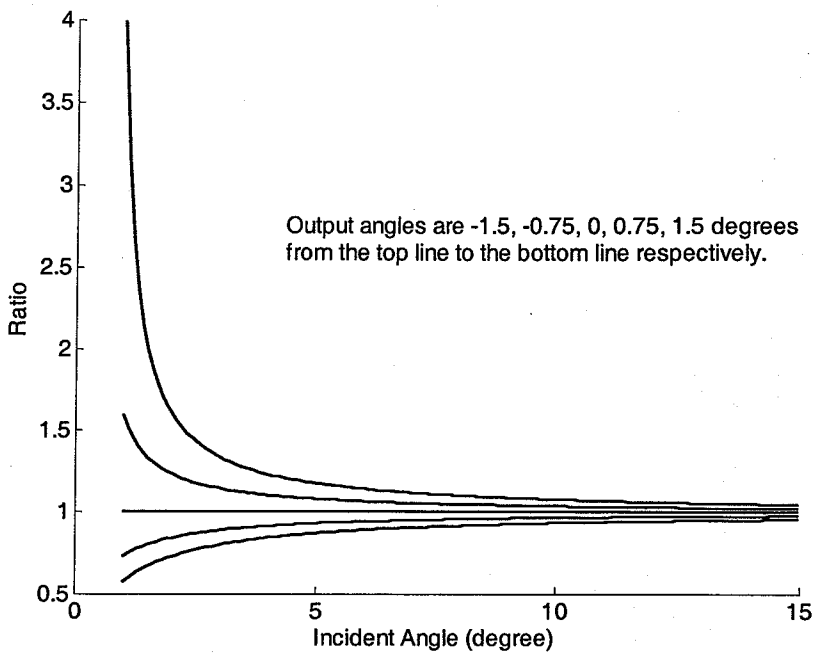

(a)

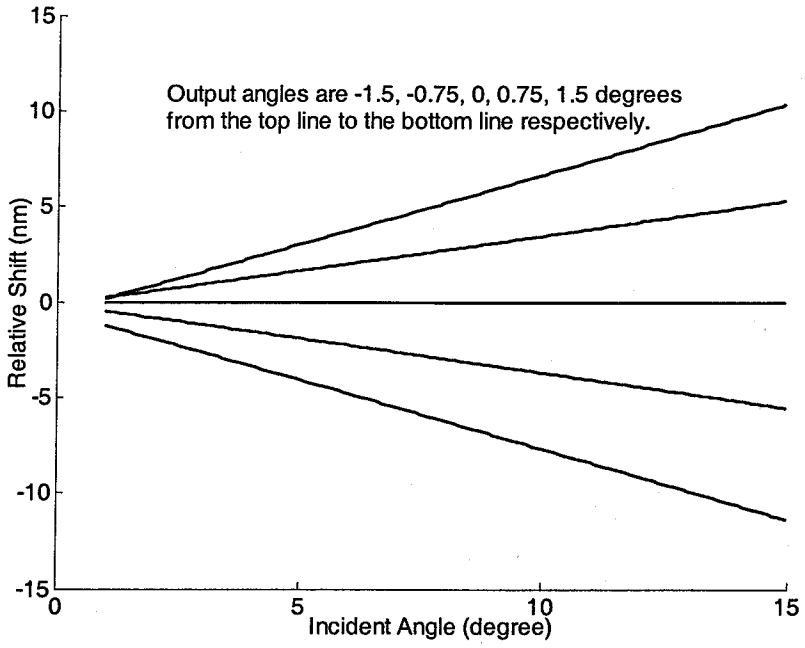

(b)

Fig. 4.2. A theoretical comparison for the two dispersion laws.

(a) is the relative ratio γ in (4.29); (b) is the wavelength shift $\Delta\lambda$ in the new dispersion law (4.22).

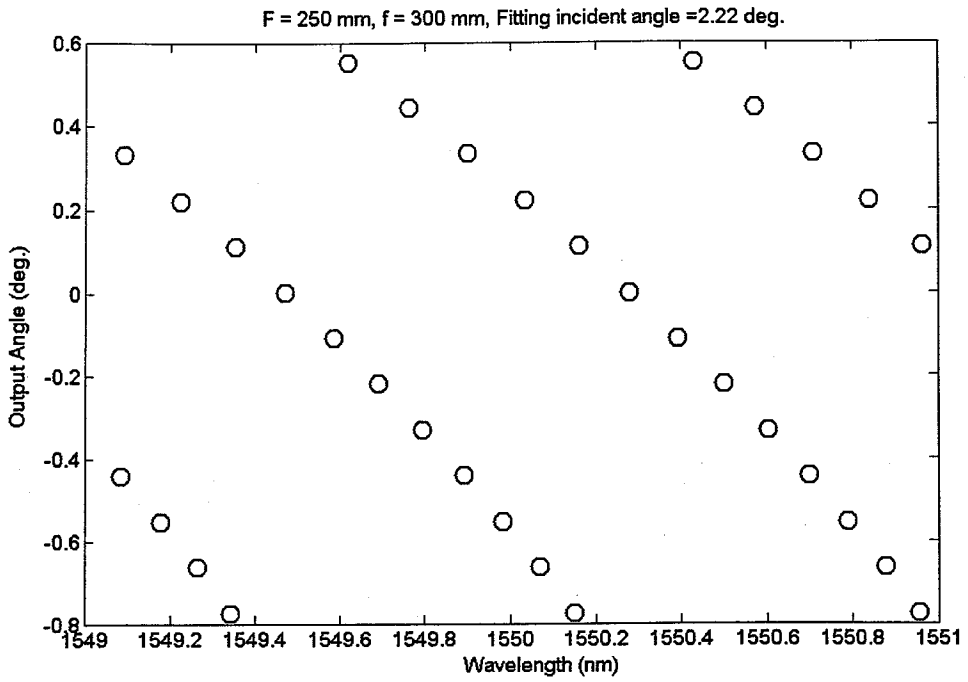
F = 250 mm, f = 300 mm, Fitting incident angle =2.22 deg.
Output Angle (deg.)
Wavelength (nm)
0.6
0.4
0.2
0
-0.2
-0.4
-0.6
-0.8
1549
1549.2
1549.4
1549.6
1549.8
1550
1550.2
1550.4
1550.6
1550.8
1551

(a)

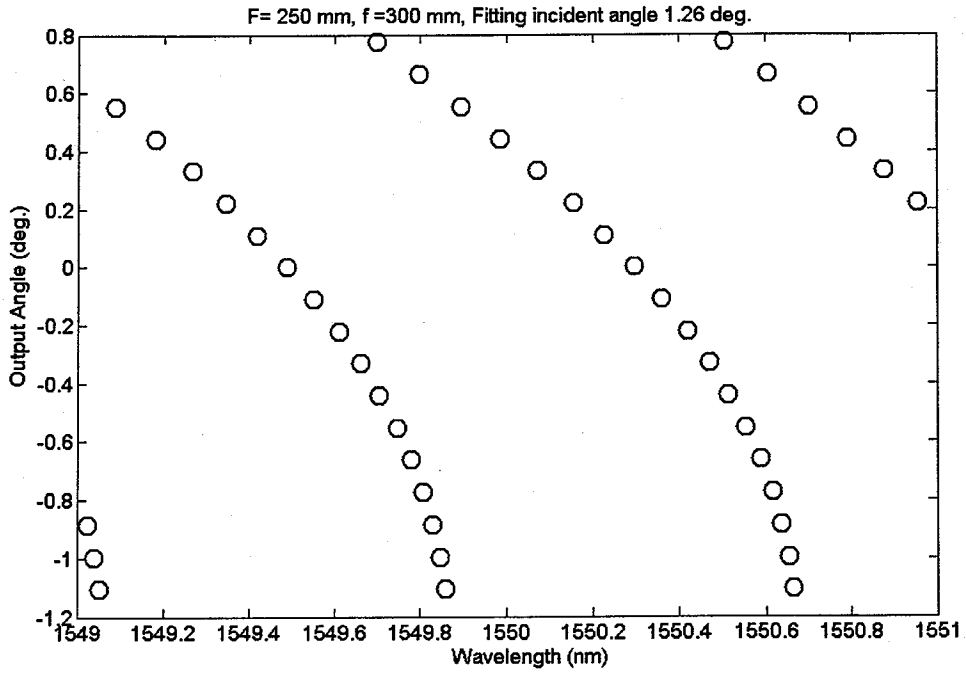
F= 250 mm, f =300 mm, Fitting incident angle 1.26 deg.
Output Angle (deg.)
Wavelength (nm)
0.8
0.6
0.4
0.2
0
-0.2
-0.4
-0.6
-0.8
-1
-1.2
1549
1549.2
1549.4
1549.6
1549.8
1550
1550.2
1550.4
1550.6
1550.8
1551

(b)

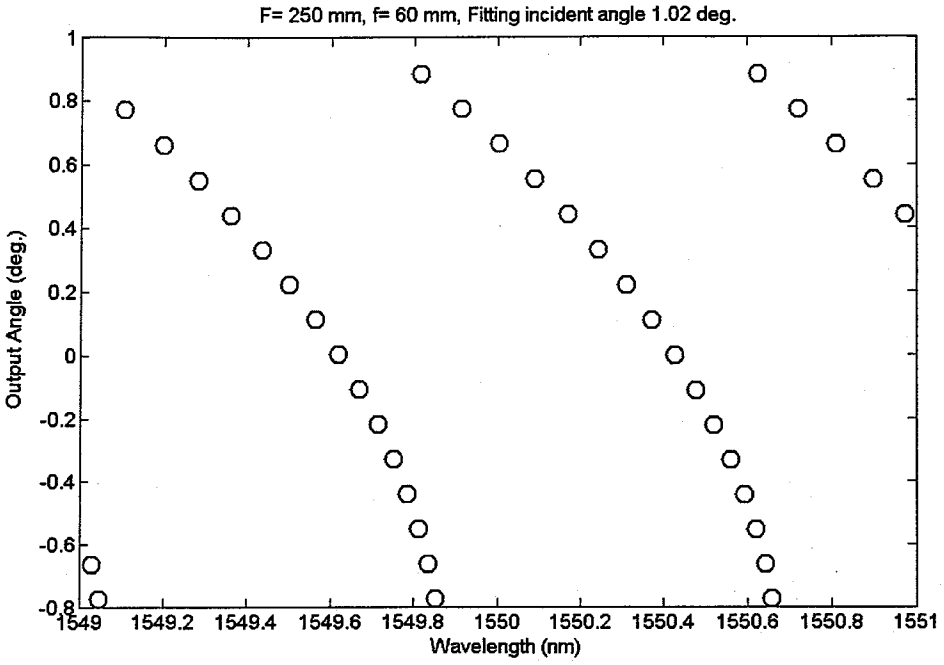

(c)

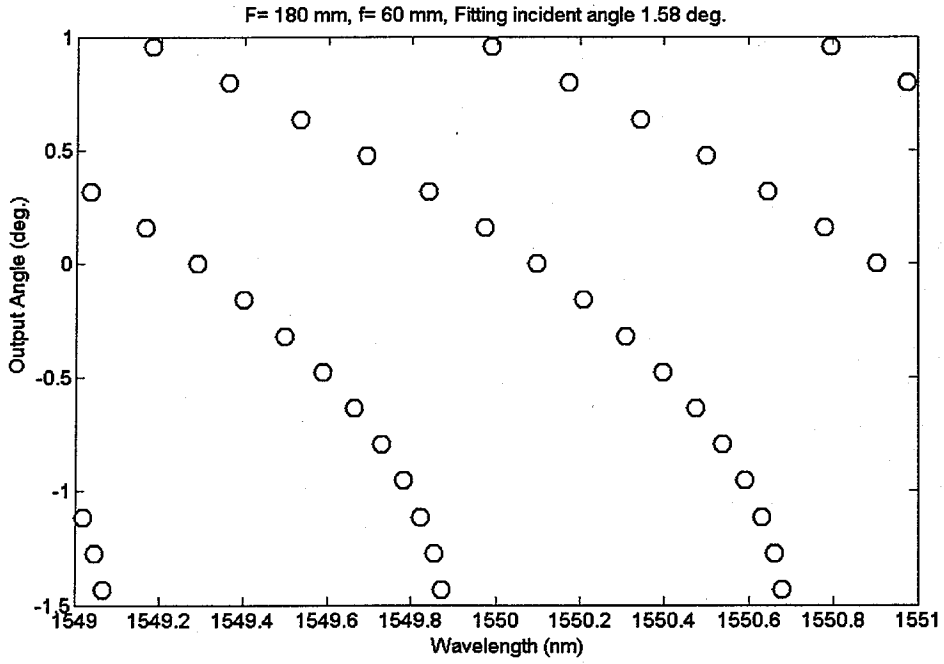

(d)

Fig. 4.3. (a) - (d): The output angle θ_o vs. wavelength λ. The dispersion is ≥ 1 degree/nm, and the spacing from one wavelength to the next is about 0.8 nm for one fixed output angle.

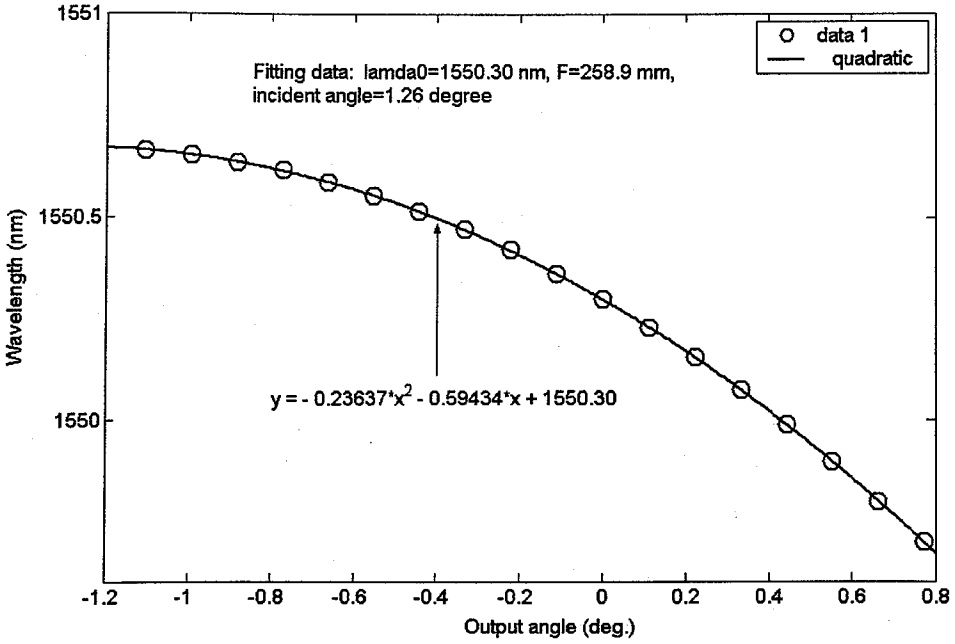

(a) CYL focal length 300 mm

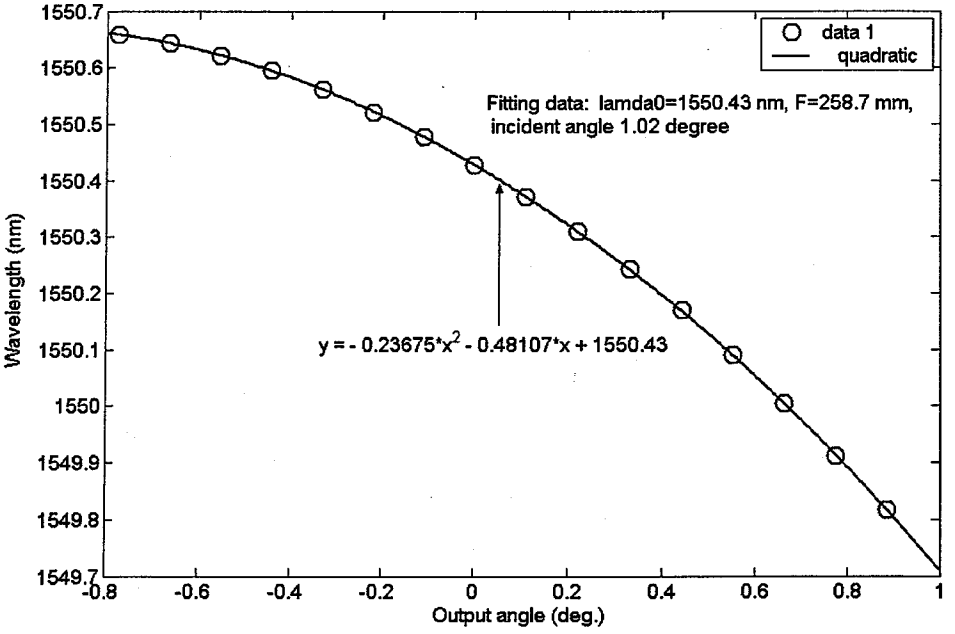

(b) CYL focal length 60 mm

Fig. 4.4. VIPA dispersion curve fitting: wavelength vs. output angle. 4.4 (a) is for 4.3 (b), and 4.4 (b) is for 4.3 (c). y, x in equations represent the wavelength and the output angle respectively.

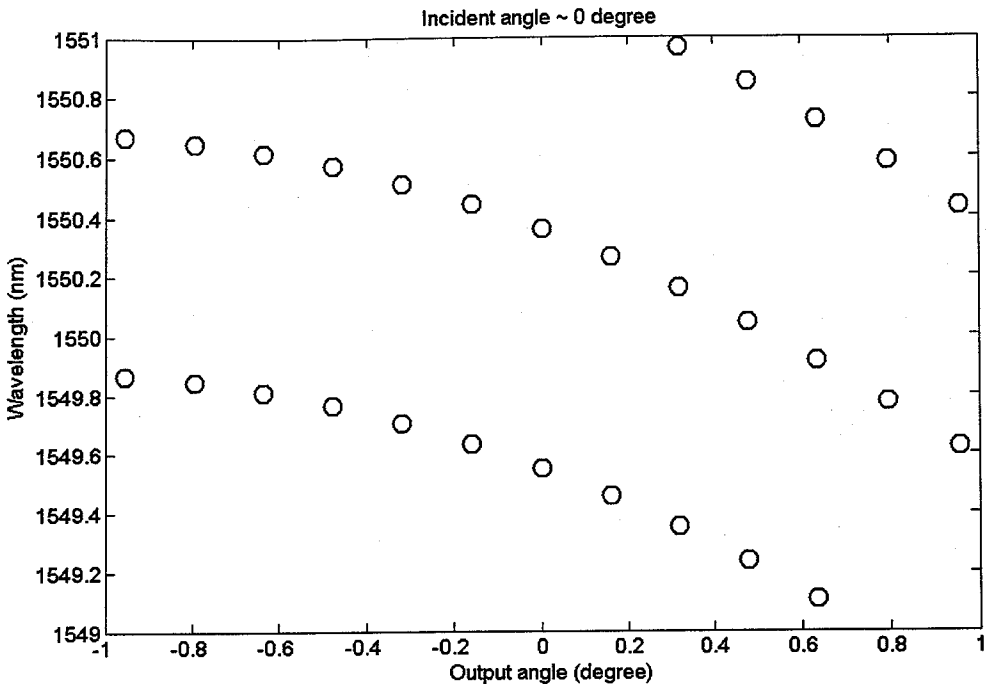
Incident angle ~ 0 degree
Wavelength (nm)
1551
1550.8
1550.6
1550.4
1550.2
1550
1549.8
1549.6
1549.4
1549.2
1549
-1
-0.8
-0.6
-0.4
-0.2
0
0.2
0.4
0.6
0.8
1
Output angle (degree)

(a)

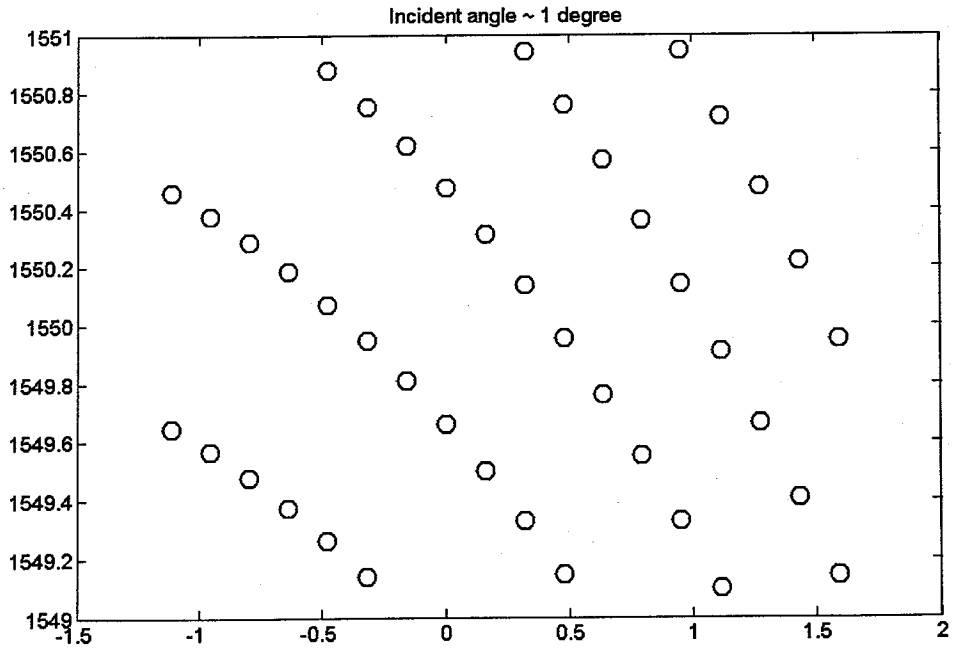
Incident angle ~ 1 degree
1551
1550.8
1550.6
1550.4
1550.2
1550
1549.8
1549.6
1549.4
1549.2
1549
-1.5
-1
-0.5
0
0.5
1
1.5
2

(b)

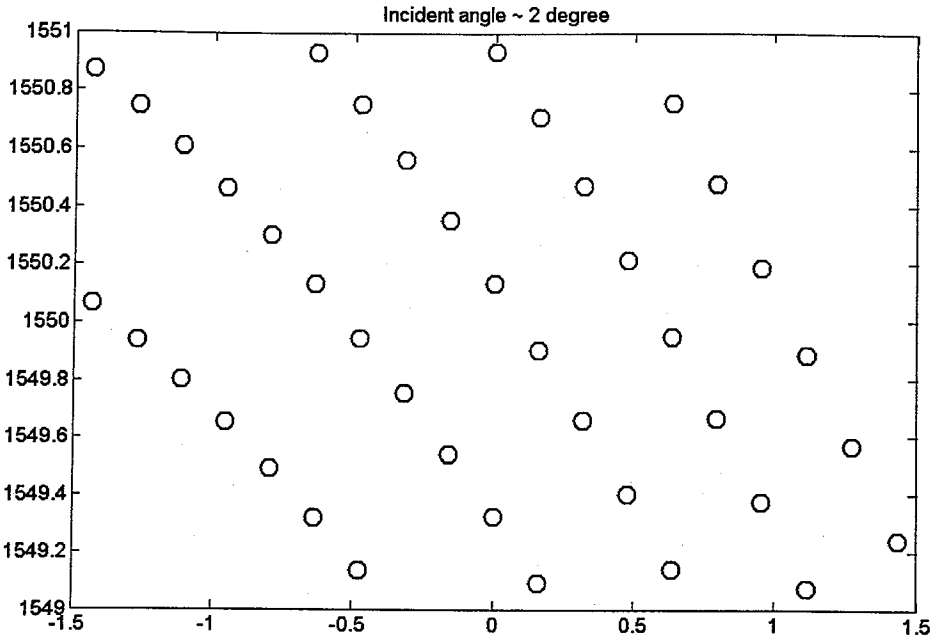

(c)

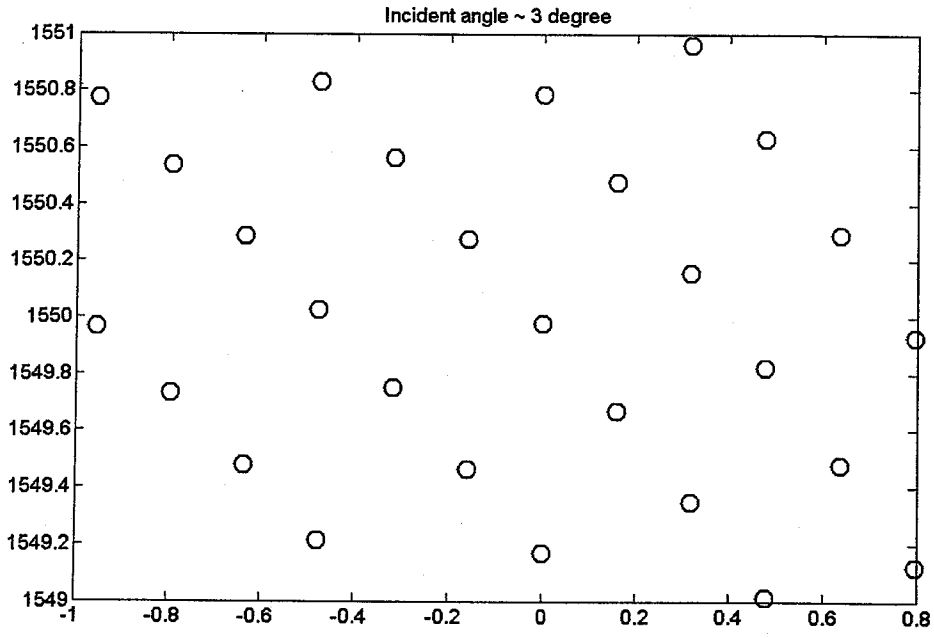

(d)

Figure 4.5. (a) – (d): The wavelength λ vs. the output angle θ_o

Another group of dispersion data for angles and thickness fitting.

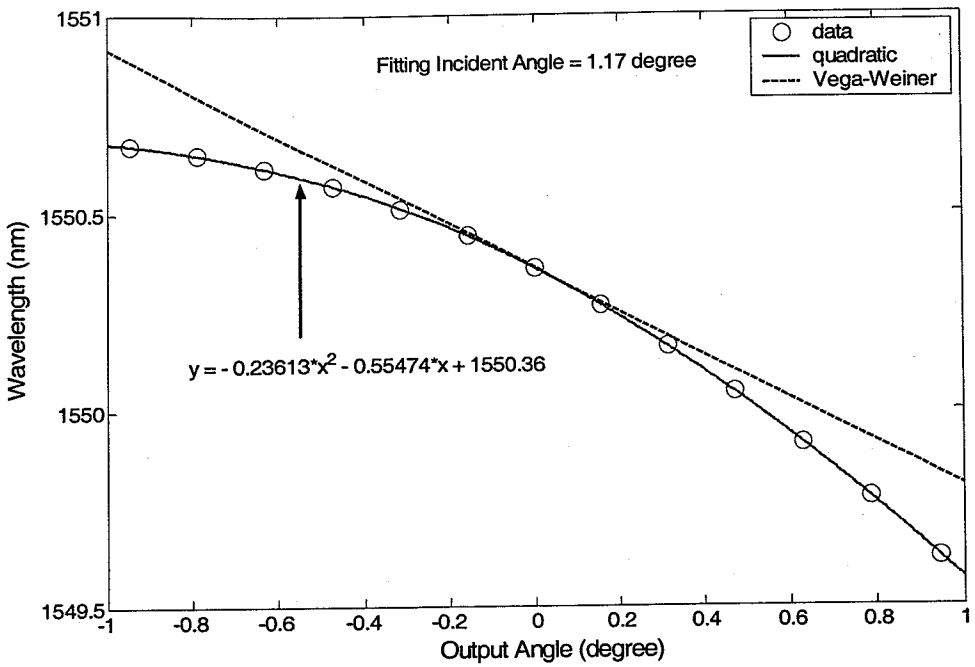
Fitting Incident Angle = 1.17 degree
data
quadratic
Vega-Weiner
y = - 0.23613*x^2 - 0.55474*x + 1550.36
Wavelength (nm)
Output Angle (degree)
1551
1550.5
1550
1549.5
-1
-0.8
-0.6
-0.4
-0.2
0
0.2
0.4
0.6
0.8
1

(a)

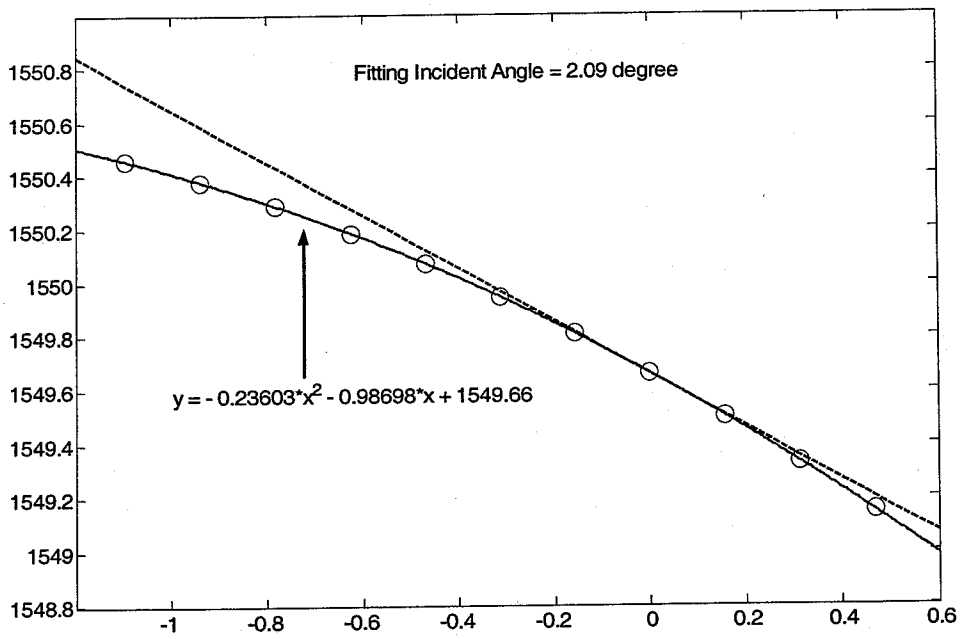
Fitting Incident Angle = 2.09 degree
y = - 0.23603*x^2 - 0.98698*x + 1549.66
1550.8
1550.6
1550.4
1550.2
1550
1549.8
1549.6
1549.4
1549.2
1549
1548.8
-1
-0.8
-0.6
-0.4
-0.2
0
0.2
0.4
0.6

(b)

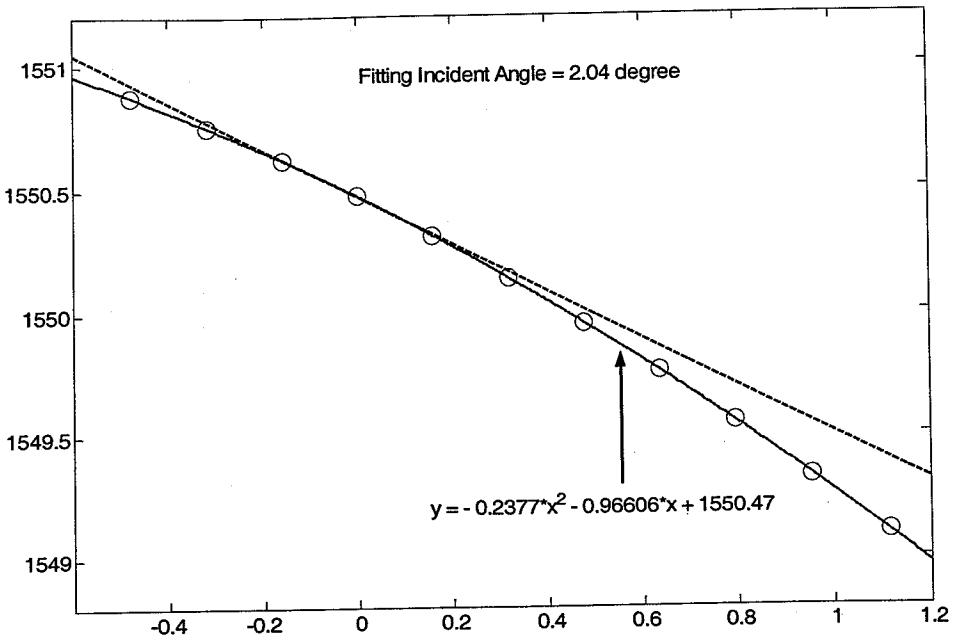
Fitting Incident Angle = 2.04 degree
y = - 0.2377*x^2 - 0.96606*x + 1550.47
1551
1550.5
1550
1549.5
1549
-0.4
-0.2
0
0.2
0.4
0.6
0.8
1
1.2

(c)

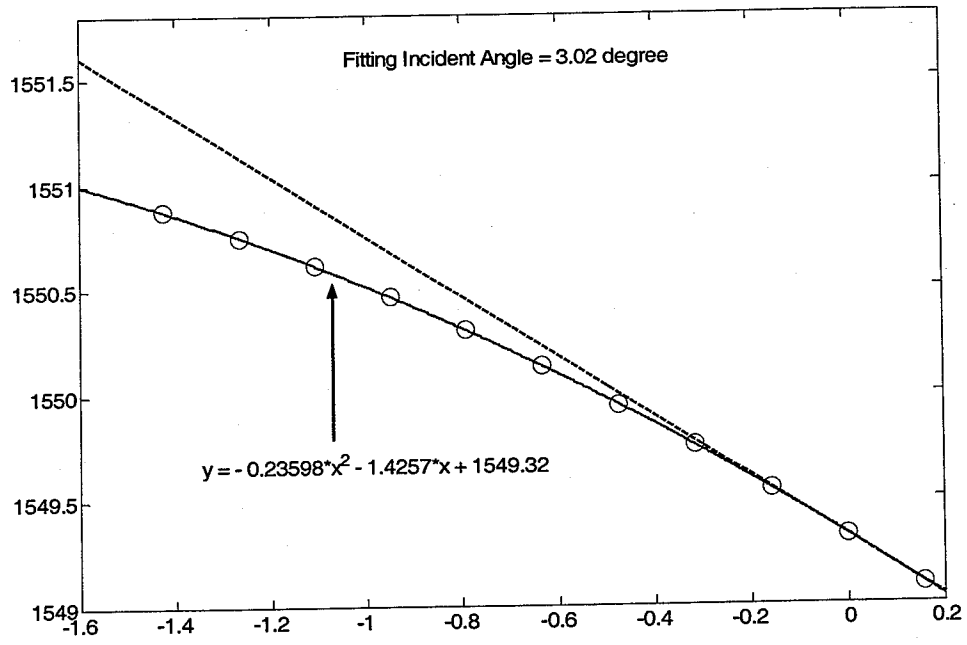
Fitting Incident Angle = 3.02 degree
y = - 0.23598*x^2 - 1.4257*x + 1549.32
1551.5
1551
1550.5
1550
1549.5
1549
-1.6
-1.4
-1.2
-1
-0.8
-0.6
-0.4
-0.2
0
0.2

(d)

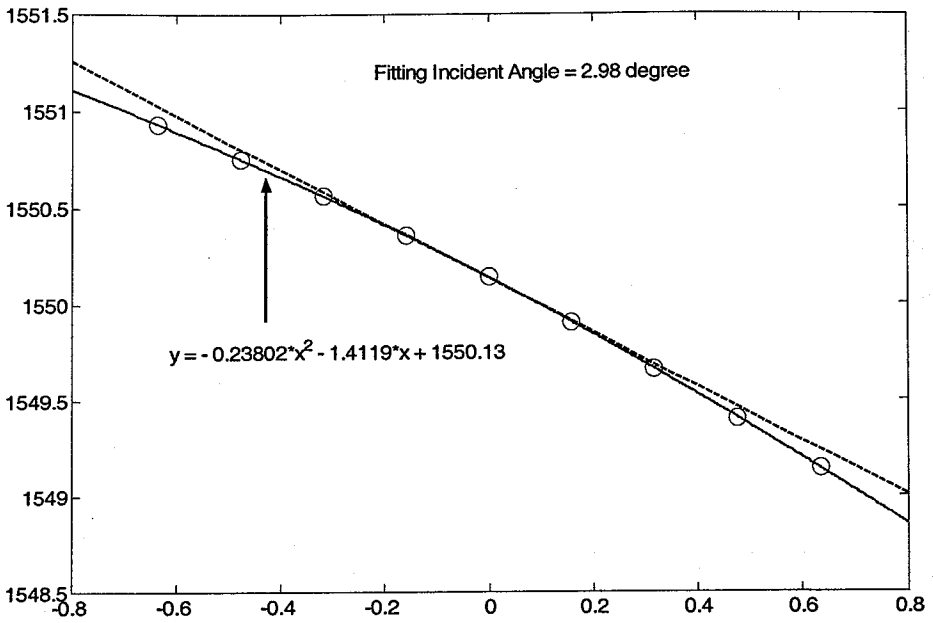
Fitting Incident Angle = 2.98 degree
y = - 0.23802*x^2 - 1.4119*x + 1550.13
1551.5
1551
1550.5
1550
1549.5
1549
1548.5
-0.8
-0.6
-0.4
-0.2
0
0.2
0.4
0.6
0.8

(e)

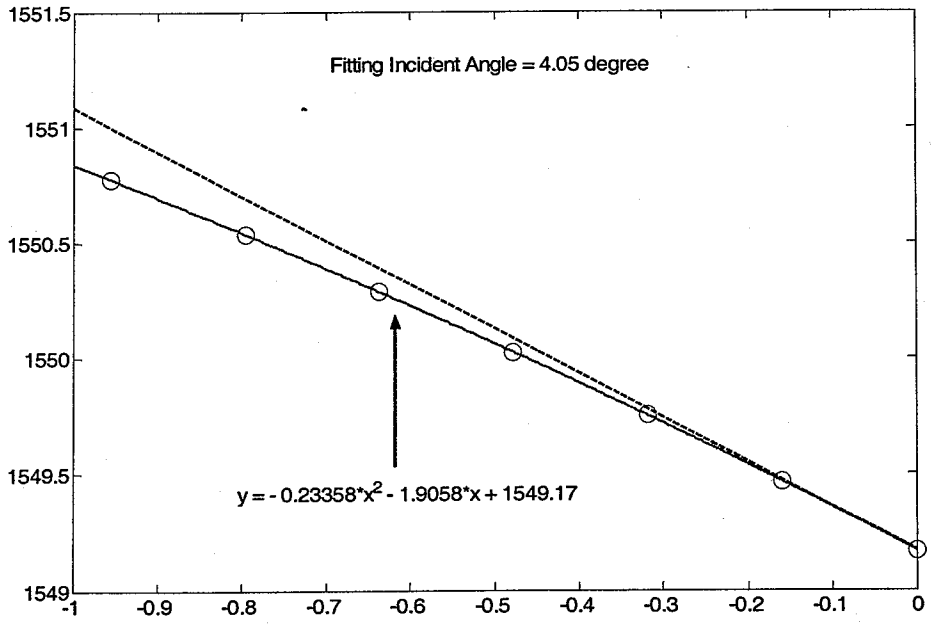
Fitting Incident Angle = 4.05 degree
y = - 0.23358*x^2 - 1.9058*x + 1549.17
1551.5
1551
1550.5
1550
1549.5
1549
-1
-0.9
-0.8
-0.7
-0.6
-0.5
-0.4
-0.3
-0.2
-0.1
0

(f)

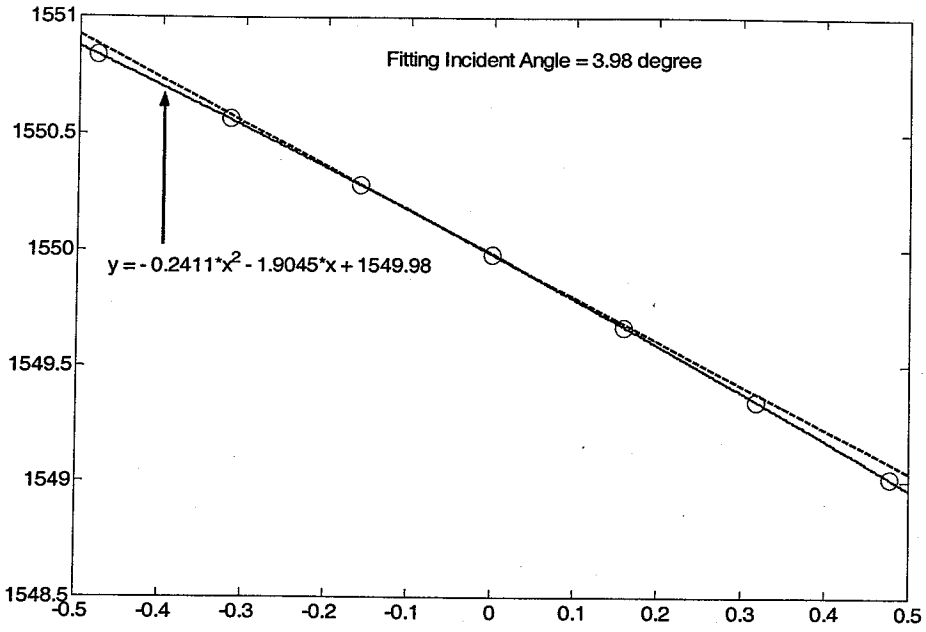

(g)

Figure 4.6. New VIPA dispersion law vs. Vega – Weiner dispersion law. (a) is for 4.5 (a); (b) and (c) are for 4.5 (b); (d) and (e) are for 4.5 (c); (f) and (g) are for 4.5 (d). y, x in equations represent the wavelength and the output angle respectively.

5. CONCLUSION

To summarize this thesis, we have studied the spectral line-shape and dispersion law of virtually imaged phased array (VIPA) demultiplexers. We demonstrate that the symmetry behavior of the VIPA demultiplexer spectrum line-shape strongly depends on the receiver's longitudinal position. We identify a spatial chirp effect strongly related to the line-shape asymmetry. The VIPA dispersion law (angular dispersion) has been studied both in theory and experiment. A novel and better dispersion law is proposed and fully verified by our experimentation. Our results are fully explained by our theory. All of this work is useful for construction of any system with a VIPA spectral disperser.

In addition, we also demonstrate the equivalence between paraxial wave equation and Fresnel scalar diffraction theory, which allows us to apply lens transforms by the diffraction integral to Gaussian beams. This is our basis for all the derivations in this thesis.

Currently, we are working on a VIPA DST pulse shaper, and one direct application of such a pulse shaper is the generation of mm waves [19, 20].

LIST OF REFERENCES

[1] M. Shirasaki, *"Large angular dispersion by a virtually imaged phased array and its application to a wavelength demultiplexer"*, Opt. Lett. 21, 366-368 (1996).

[2] M. Shirasaki, IEEE Phot. Tech. Lett. 11, 1443-1445 (1999).

[3] M. Shirasaki, IEEE Phot. Tech. Lett. 9, 1598-1560 (1997).

[4] M. Shirasaki, Optical Fiber Communication Conference, TuS1-3, 2001.

[5] M. Shirasaki, "Virtually imaged phased array (***VIPA***) having air between reflecting surfaces", Patent No. 5,969,866, Oct. 19, 1999.

[6] M. Shirasaki, "Optical apparatus which uses a virtually imaged phased array to produce chromatic dispersion", Pub. No. US 20030021046, Jan. 30, 2003.

[7] C. Lin, M.S. Thesis, MIT, June, 2000.

[8] A. Vega, M.S. Thesis., Purdue University, December, 2002.

[9] A. Vega, A. M. Weiner, C. Lin, *"Generalized grating equation for virtually-imaged phased-array spectral dispersers"*, Appl. Opt. in press, Vol. 42, No .20, Jul., 2003.

[10] J. W. Goodman, *Introduction to Fourier Optics, 1964.*

[11] H. A. Haus, *Waves and Fields in Optoelectronics, 1984.*

[12] Simon Ramo, *Fields and waves in communication electronics,* 1994.

[13] H. Kogelnik, "*Laser beams and resonators*", *Appl. Opt* ., 5, 1550-1556, Oct., 1966.

[14] J. T. Verdeyen, *Laser Electronics*, 1995.

[15] D. E. Leaird, A. M. Weiner, *"Femtosecond Direct Space-to-Time Pulse Shaping"*, IEEE J. Q. E., Vol. 37, No. 4, April 2001.

[16] D. E. Leaird, A. M. Weiner, *"Chirp control in the direct space-to-time pulse shaper"*, Opt. Lett., Vol. 25, No. 11, June, 2000.

[17] D. E. Leaird, A. M. Weiner, *"Femtosecond optical packet generation by a direct space-to-time pulse* shaper", Opt. Lett., Vol. 24, No. 12, June, 1999.

[18] S. Xiao, A. M. Weiner, C. Lin, *"Spatial Chirp Effect in Virtually Imaged Phased Array Wavelength Demultiplexers"*, CWP6, *Conference on Lasers and Electro Optics* (CLEO) 2003.

[19] J. D. McKinney, D. S. Seo, S. Xiao, A. M. Weiner, *"Photonically-assisted Arbitrary Millimeter Waveform Generation"*, Photonics Time/Frequency Measurement and Control, MC4.3, Lasers & Electro-Optics Society (LEOS) Summer Topical Meetings 2003.

[20] J. D. McKinney, D. E. Leaird, and A. M. Weiner, *"Millimeter-wave Arbitrary Waveform Generation with a Direct Space-to-Time Pulse Shaper"*, Opt. Lett. Vol. 27, pp. 1345-1347, 2002.